Supporting Information for

Unravelling the Major Factors in Photo-oxidative Stability of Anthradithiophene Derivatives.

Karl J. Thorley,[1]* Hoang Le,[2] Yang Song,[2] John E. Anthony[1,3]

[1]University of Kentucky, Center for Applied Energy Research, Lexington KY 40511, USA
[2]Centre College, Department of Chemistry, Danville KY 40422, USA
[3]University of Kentucky, Department of Chemistry, Lexington KY 40508, USA

Contents

General Information

Materials were synthesised as previously reported: TES-ADT,[1] TES-FADT,[2] TES-EtADT,[3] TNPC-FADT,[4] TIPS-CNADT,[5] TIPS-PN.[6] Synthesis of TES-OMeADT is reported in the synthesis section below. Methylene blue was purchased from J.T. Baker.

UV-Vis spectroscopy was performed using a Cary 60 spectrometer in a 10mm cuvette in chloroform (Alfa Aesar, 32614, stabiliser-free). Chloroform was used as the solvent for several reasons; the time scale for photodecomposition was expected to be fairly fast for chlorinated solvents,[7] a relatively high boiling point would minimise solvent evaporation, chloroform is a common NMR solvent, and also provides reasonable solubility for methylene blue. Some experiments were repeated with toluene (Macron Chemicals, MK860822).

During photodecomposition experiments, samples were illuminated from above by LED light sources from a StellarNet Inc SilverNova spectrophotometer. Absorption spectra were then automatically collected at 5 minute intervals using the cycle mode of the spectrometer with the chamber partially open. To allow the samples to absorb the LED light, the cuvette was covered with a glass slide held in place with 3M mounting putty at the edges of the cuvette. A "dark" experiment under identical conditions but with no LED light showed no significant change in absorbance, therefore solvent loss by evaporation is minimal over the experimental time frame, and the ADT chromophores are stable in the small amount of residual room lighting from the partially open lid. The light source was held in place by a clampstand such that the bottom of the LED was consistently 3 cm above the glass-covered cuvette. All samples were measured in a total volume of 3.0 mL, providing a consistent vertical "path length". Initial rate experiments were conducted in an identical manner, except that the Cary kinetics software was used to monitor a single wavelength (λ_{max} for the relevant chromophore) over 10 minutes with 1 second intervals between data points. Absorption stayed above 90% of the initial absorbance over this time frame. A linear fit was used to extract initial reaction rates.

The spectral shape of the light sources was determined by shining the light into a StellarNet Inc SilverNova spectrophotometer in scope mode, although the exact intensity could not be reliably determined. The comparison of these different light sources with the chromophores are shown next to the relevant photodecomposition data.

Extinction coefficients were measured by making stock solutions of 10-20 mg in 50 or 100 mL volumetric flasks, and making UV-Vis samples with aliquots of this stock sample. Linear fits of absorbance versus concentration were used to establish adherence to Beer's law over the concentration range used in subsequent experiments, as well as deriving the extinction coefficient from the slope of the fit. Further samples used for photooxidation experiments were adjusted by their absorbance rather than the amount of stock solution added to avoid any issues of changes in stock concentration by solvent loss.

Cyclic voltammetry was measured using a BAS CV-50W potentiostat at a scan rate of 50 mV/s with a button glassy carbon working electrode, a platinum wire counter electrode and an Ag/AgCl reference electrode. A solution of 0.1 M Bu$_4$NPF$_6$ in dichloromethane was used as a supporting electrolyte solution under a blanket of N$_2$ with Fc/Fc$_+$ as an internal reference. Although literature values are known for these materials, all electrochemical measurements were repeated to ensure consistency between measurement conditions.

Proton and carbon NMR spectra were collected using a 400 MHz JEOL spectrometer at 298 K. Chemical shifts of each spectrum are reported in ppm and referenced to deuterated chloroform solvent.

Density functional theory (DFT) calculations were carried out using Gaussian 16 Rev A.03 software,[8] and further details are discussed in the relevant section.

Synthesis of TES-OMeADT
1-Iodothiophene-3,4-carboxaldehyde

Thiophene-2,3-dicarboxaldehyde (1.27 g, 9.07 mmol) was dissolved in $CHCl_3$ (60 mL). BTI ([bis(trifluoroacetoxy)iodo]benzene) (3.1 g , 7.26 mmol) and iodine (1.84 g, 7.26 mmol) were added and the reaction stirred at room temperature overnight. The reaction mixture was analysed by GC-MS, and additional 0.1 equivalents of BTI and iodine were added if the reaction was not complete, and stirred for a further hour. Once the reaction was complete, the reaction mixture was transferred to a separatory funnel and washed with 0.1 M KOH(aq) (3 × 50 mL). The solvent was removed under reduced pressure. The crude product was suspended in hexanes and poured onto a silica plug, eluting with hexanes to remove fast running impurities, and then CH_2Cl_2 to elute the product, yielding a pale yellow powder after removal of solvent (1.80g, 75 %)

^{1}H NMR (400 MHz, $CDCl_3$) δ 10.33 (1H, s), 10.23 (1H, s), 7.77 (1H, s)

^{13}C NMR (100 MHz, $CDCl_3$) δ 183.2, 181.2, 152.7, 144.4, 139.5, 86.4

HRMS (ESI, +ve) calculated for C_6H_3OINaS: 288.8791. Found: 288.8796

1-Methoxythiophene-3,4-dicarboxaldehyde:
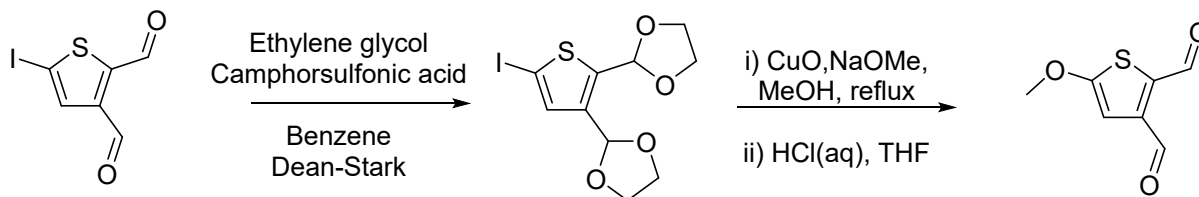
Iodothiophene dialdehyde (2.01 g, 7.55 mmol) was dissolved in benzene (100 mL). Ethylene glycol (1.06 mL, 18.89 mmol) and camphorsulfonic acid (0.02 g, 0.09 mmol) were added and a Dean-Stark trap attached to the flask. The mixture was heated at reflux overnight. At room temperature, saturated $NaHCO_3$(aq) (100 mL) and EtOAc (100 mL) were added. The organic layer was separated and washed further with saturated $NaHCO_3$(aq) (2 × 100 mL) and then H_2O (100 mL). The organic layer was dried with

MgSO$_4$ and filtered. Removal of the solvent gave the iodothiophene diacetal (2.30 g, 86%) as a pale yellow oil which was used without further purification.

Iodothiophene diacetal (2.30 g, 6.49 mmol) was dissolved in NaOMe solution (0.5M in MeOH, 52 mL, 26.0 mmol) and Copper(II) oxide (0.26 g, 3.25 mmol) was added. The mixture was heated at reflux for 16 hours. At room temperature, water was added and the solid residue removed by filtration, washing with CH$_2$Cl$_2$. The mixed phase filtrate was transferred to a separating funnel and the organic layer collected, which was washed further with water (50 mL). The solvent was removed under reduced vacuum, and the residue redissolved in THF (50 mL). 10 % aqueous HCl (50 mL) was added, and the mixture stirred vigorously for 16 hours. The product was extracted with CH$_2$Cl$_2$ and washed with H$_2$O. The product was purified by silica plug (CH$_2$Cl$_2$) to yield a pale yellow solid (0.35 g, 32 %)

^{1}H NMR (400 MHz, CDCl$_3$) δ 10.35 (1H, s), 10.32 (1H, s), 6.72 (1H, s), 4.02 (6H, s)

^{13}C NMR (101 MHz, CDCl$_3$) δ 184.2, 181.3, 174.0, 143.9, 134.8, 105.9, 60.9

HRMS (ESI, +ve) calculated for C$_7$H$_6$O$_3$NaS: 192.9930. Found: 192.9934

2,8-Dimethoxy anthradithiophene quinone:
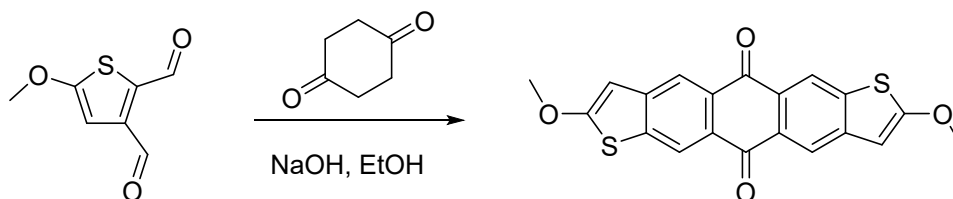
Methoxy thiophene dialdehyde (0.35 g, 2.06 mmol) was dissolved in a minimum volume (c.a. 10 mL) of hot ethanol and allowed to cool to room temperature. 1,4-Cyclohexanedione (0.105 g, 0.94 mmol) as added before very careful dropwise addition of 15% NaOH (aq) until a brown solid formed (c.a. 0.05 mL). This mixture was stirred for 1 hour at room temperature and then filtered, washing with MeOH, acetone and Et$_2$O. This yielded the quinone (mixture of *syn*- and *anti*- isomers) as a brown powder (0.15 g, 42%) which was identified by mass spectrometry but was not soluble enough for ^{1}H NMR analysis.

HRMS (ESI, +ve) calculated for C$_{20}$H$_{13}$O$_4$S$_2$: 381.0250. Found: 381.0251

2-8-Dimethoxy-bis-5,11-(triethylsilylethynyl)anthradithiophene:
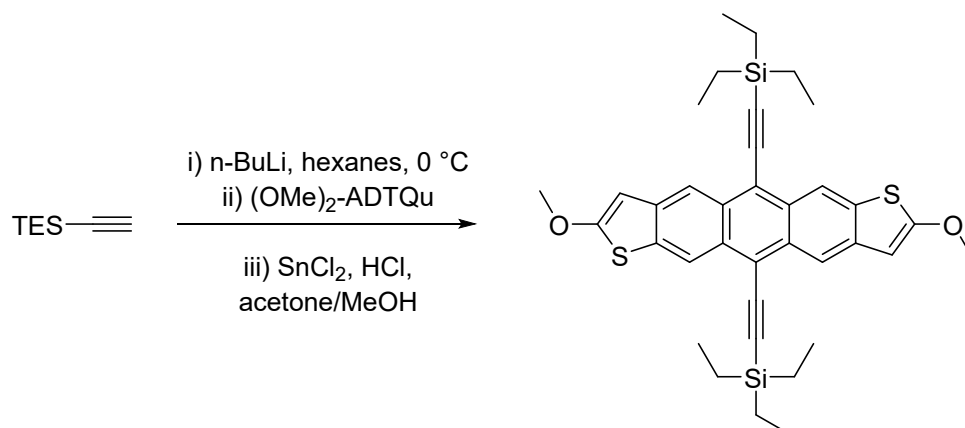
Triethylsilyl acetylene (0.24 mL, 1.31 mmol) was dissolved in hexanes (25 mL) under N_2 and cooled to 0 °C. n-Butyllithium (2.5M in hexanes, 0.42 mL, 1.04 mmol) was added slowly and the reaction stirred at 0 °C for 1 hour. Dimethoxyanthradithiophene quinone (0.100 g, 0.26 mmol) was added to the mixture which was subsequently stirred for 16 hours at room temperature. The reaction was quenched with a few drops of saturated NH_4Cl (aq) solution. The crude mixture was passed through a silica plug, eluting with hexanes to remove excess alkyne and then 1:1 CH_2Cl_2/acetone to elute the anthradithiophene diol intermediate. After solvent removal, this intermediate was redissolved in acetone (50 mL). MeOH (50 mL), Tin(II) chloride (0.30 g, 1.31 mmol) and 10% HCl(aq) (20 mL) were added, and the reaction stirred for 1 hour. H_2O (50 mL) and CH_2Cl_2 (50 mL) were added and the organic layer separated. The crude mixture was passed through a silica plug (2:1 hexanes/CH_2Cl_2). The dimethoxy anthradithiophene (a mixture of *syn-* and *anti-* isomers) was recrystallised from acetone to yield dark red needles (0.14 g, 86 %).

^{1}H (400 MHz, CDCl$_3$) δ 8.83 (2H, s), 8.67 (2H, s), 6.38 (2H, s), 4.08 (6H, s), 1.22 (18H, m), 0.90 (12H, m)

^{13}C NMR (101 MHz, CDCl$_3$) δ 166.9, 139.6, 139.4, 134.6, 134.3, 130.5, 130.0, 129.3, 128.8, 119.5, 119.3, 117.9, 117.7, 116.3, 116.2, 116.0, 105.8, 103.7, 96.6, 59.8, 7.9, 4.8

HRMS (ESI, +ve) calculated for $C_{36}H_{42}O_2S_2Si_2$: 626.2159. Found: 626.2189

Spectra for methoxyADT and intermediates
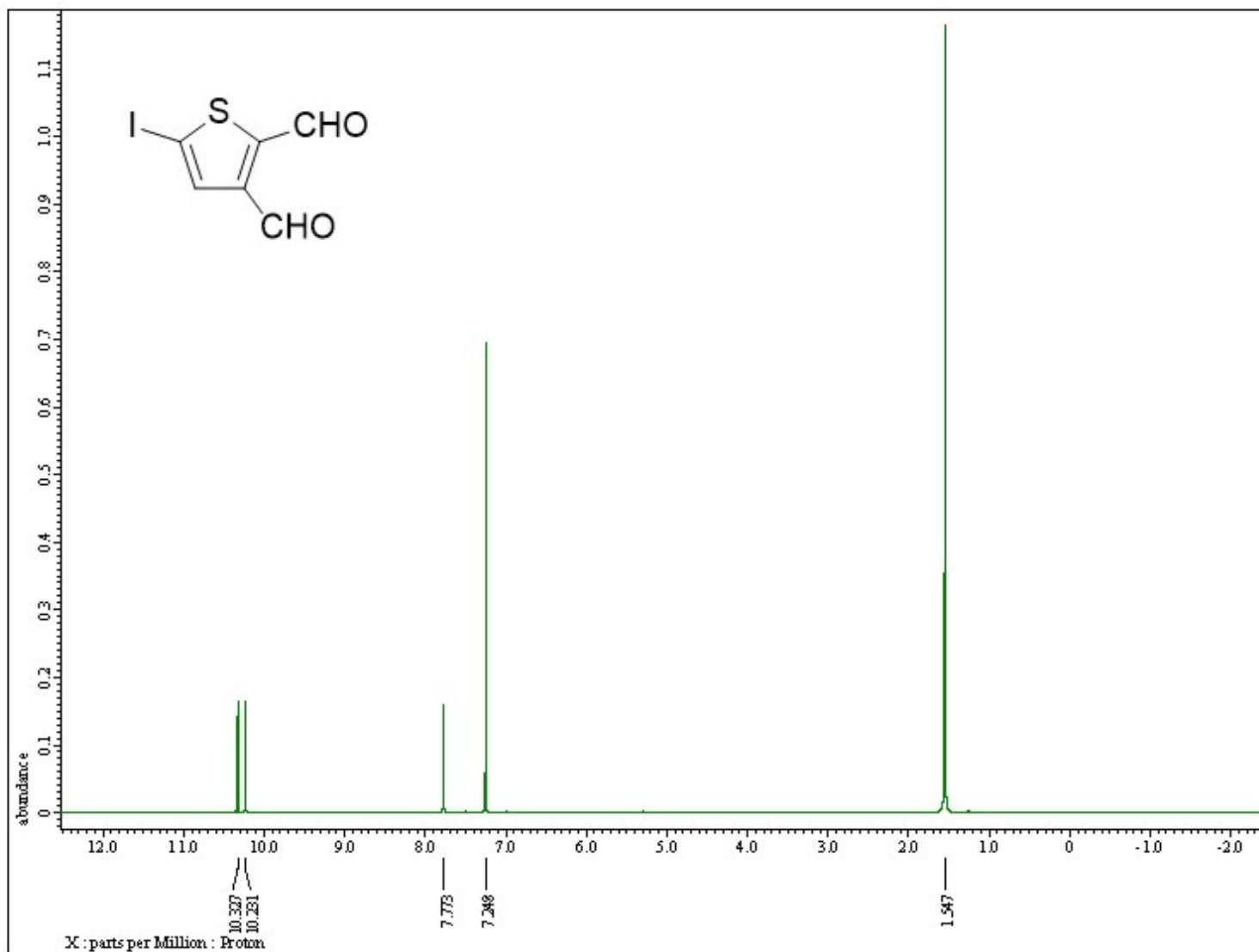
Figure S 1 ^{1}H NMR of iodothiophene dialdehyde measured in CDCl$_3$ at 298 K.
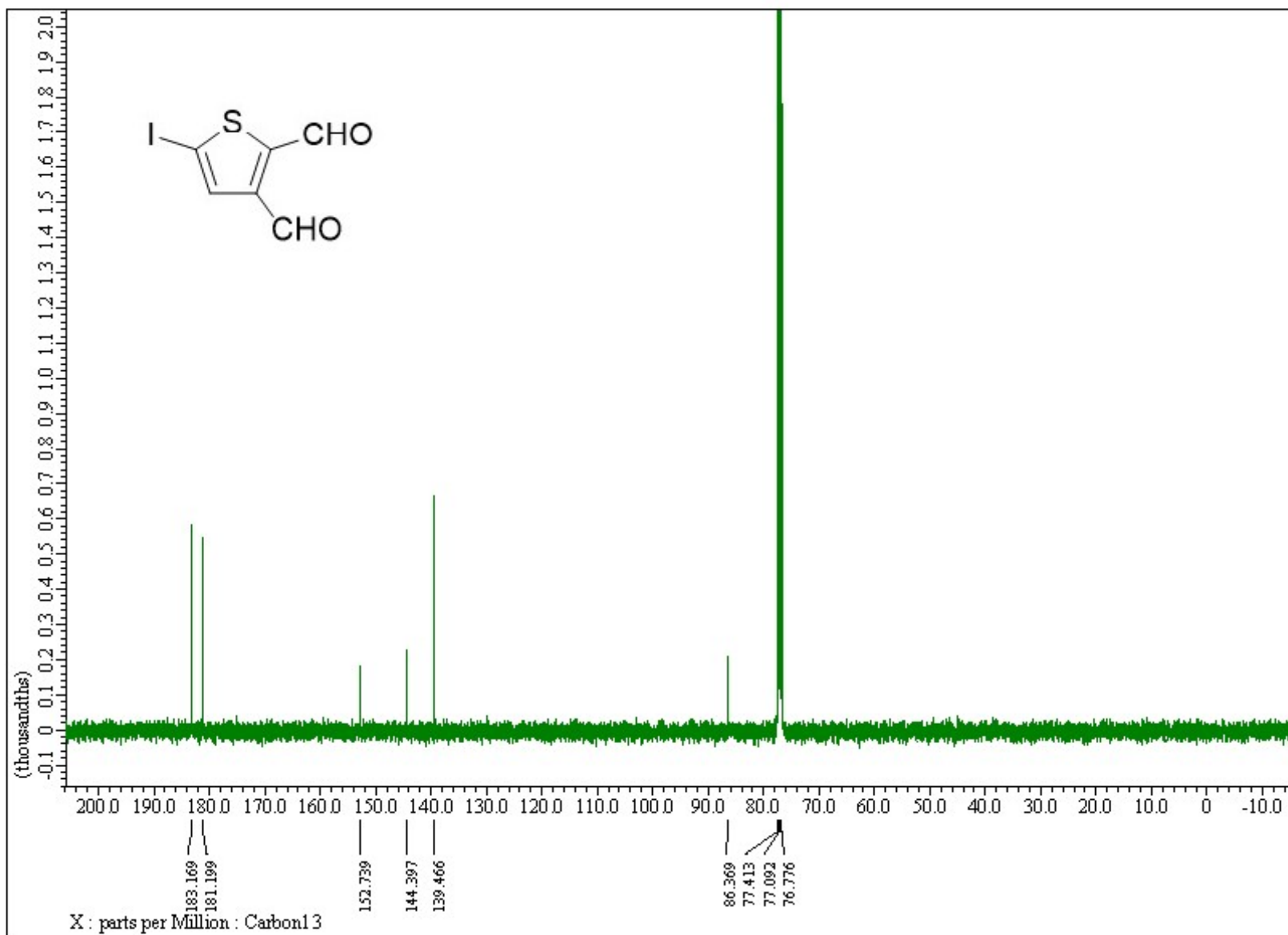
Figure S 2. ^{13}C NMR of iodothiophene dialdehyde measured in CDCl$_3$ at 298 K

I-TDA_070122d #16-27   RT: 0.46-0.77   AV: 12   NL: 4.01E6
T: FTMS + p ESI Full lock ms [120.0000-800.0000]

288.8796
$C_6 H_3 O_2 I Na S = 288.8791$
1.8760 ppm
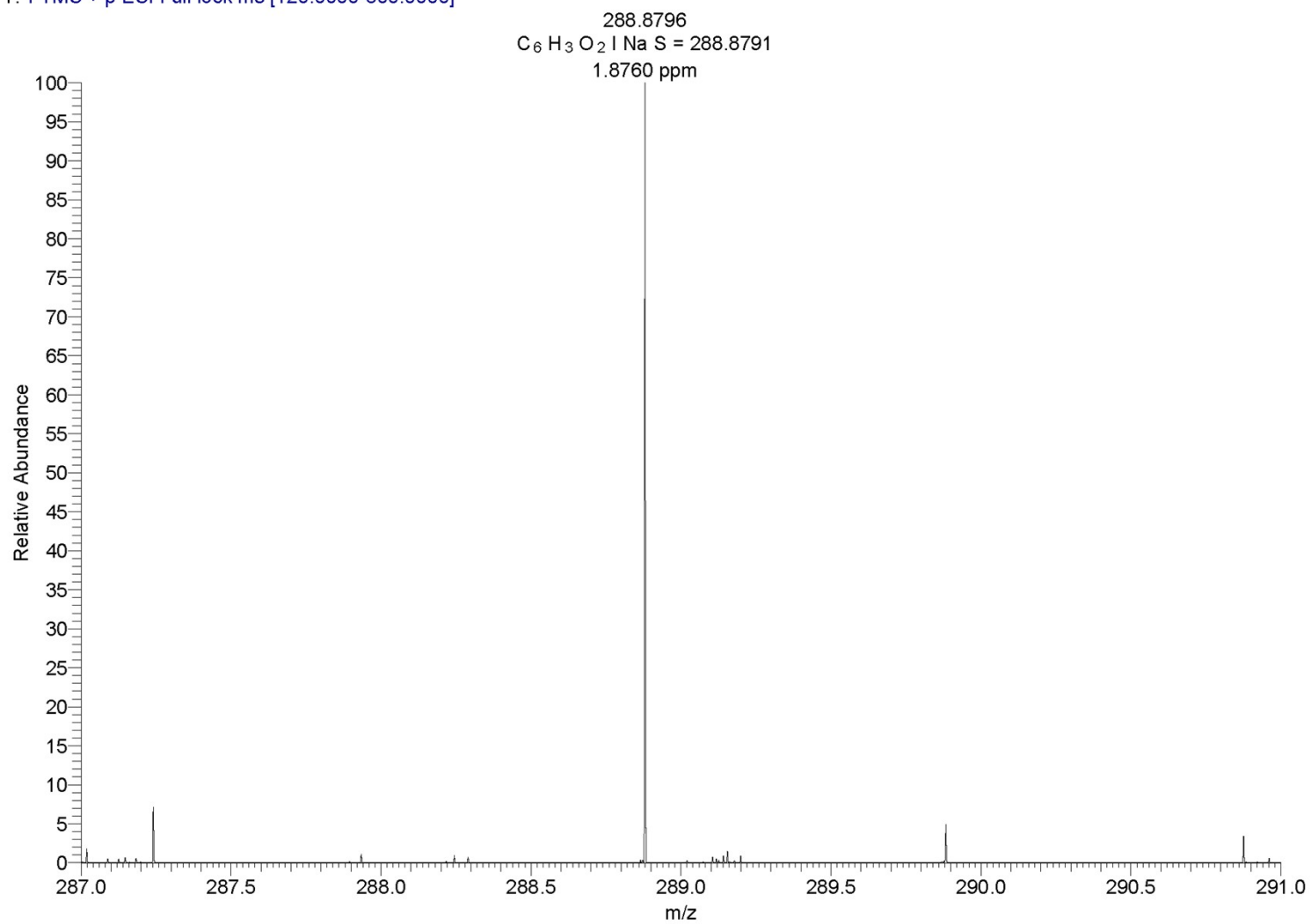
Figure S 3 HRMS ESI mass spectrum of iodothiophene dialdehyde
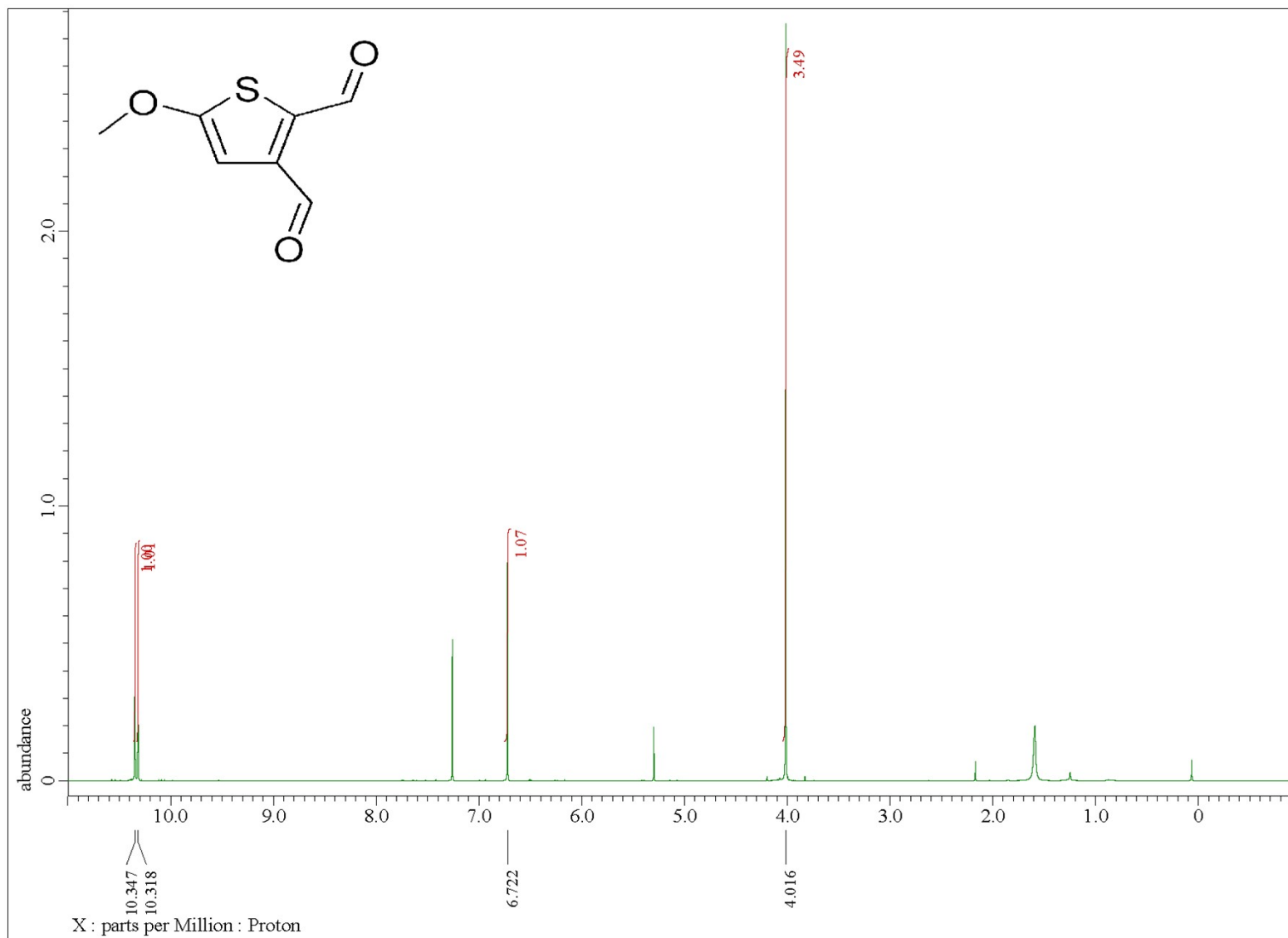
Figure S 4. ^{1}H NMR of methoxythiophene dialdehyde measured in CDCl$_3$ at 298 K.
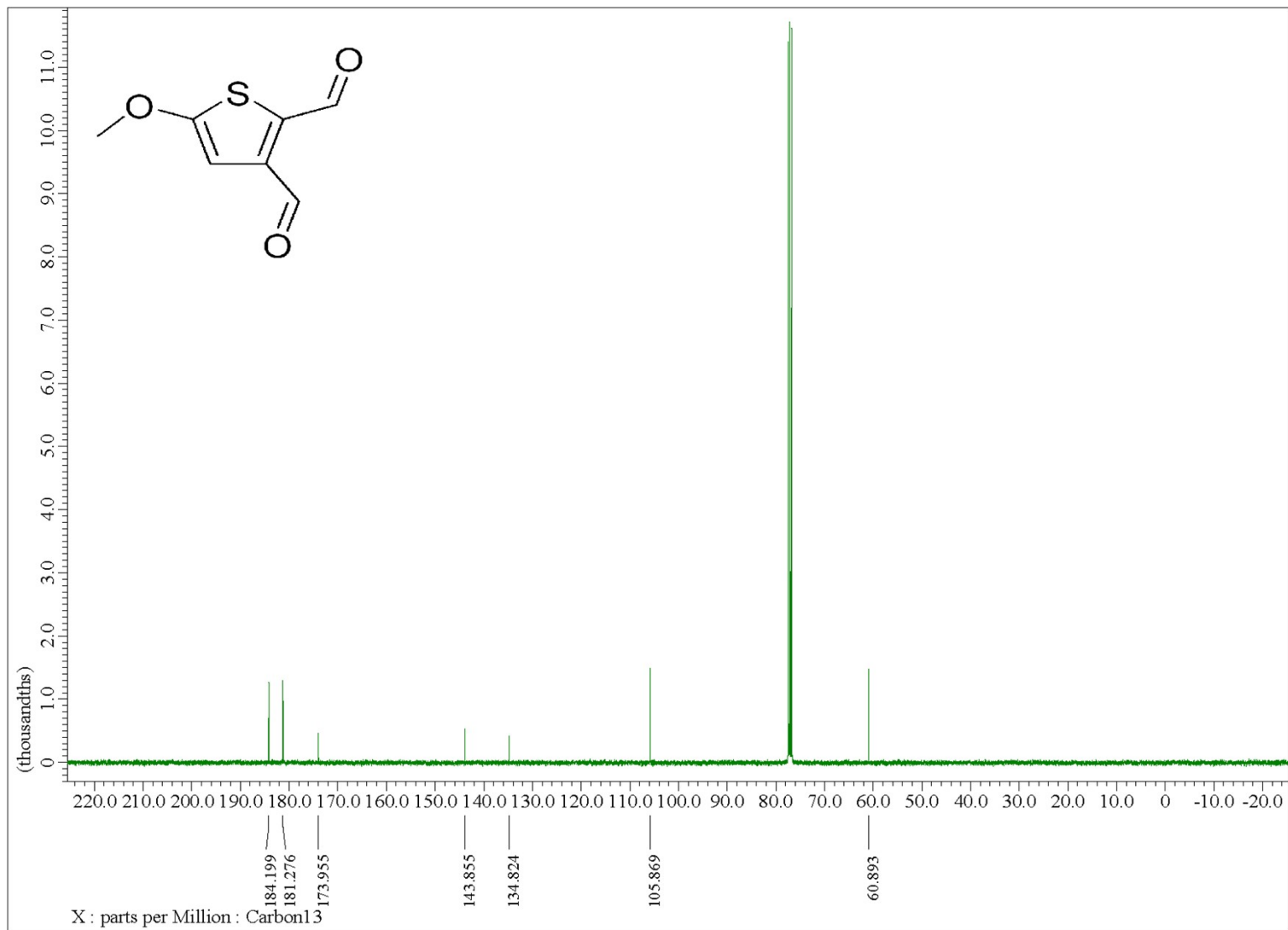
Figure S 5. ^{13}C NMR of methoxythiophene dialdehyde measured in CDCl$_3$ at 298 K.

OMe-TDA_070122d #49-76 RT: 1.40-2.17 AV: 28 NL: 8.26E7
T: FTMS + p ESI Full lock ms [120.0000-800.0000]

192.9934
$C_7 H_6 O_3 Na S = 192.9930$
1.9606 ppm
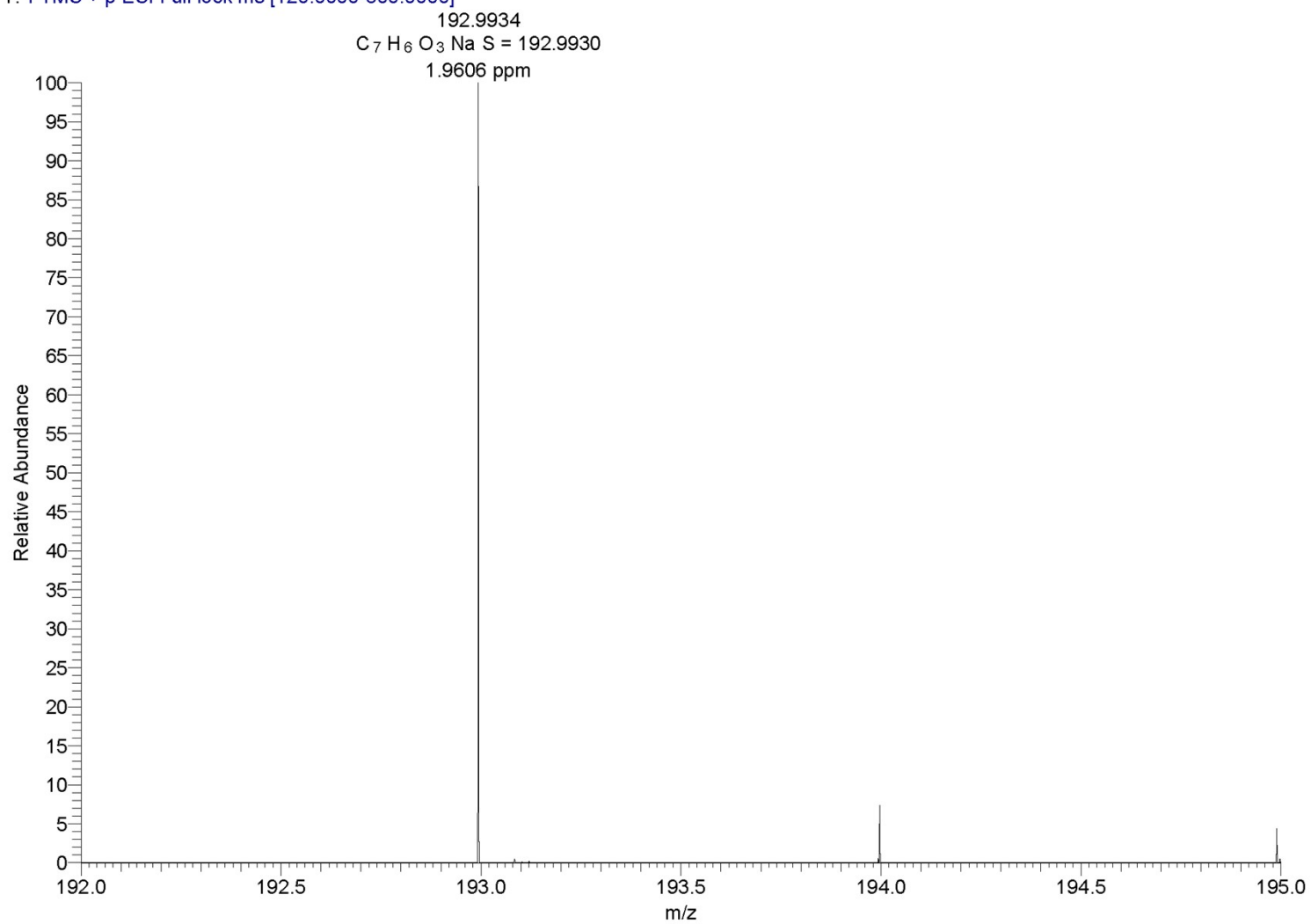
Figure S 6. HRMS ESI mass spectrum of methoxythiophene dialdehyde

OMe-Qu_070122c #20-37   RT: 0.58-1.06   AV: 18   NL: 6.48E6
T: FTMS + p ESI Full lock ms [120.0000-800.0000]
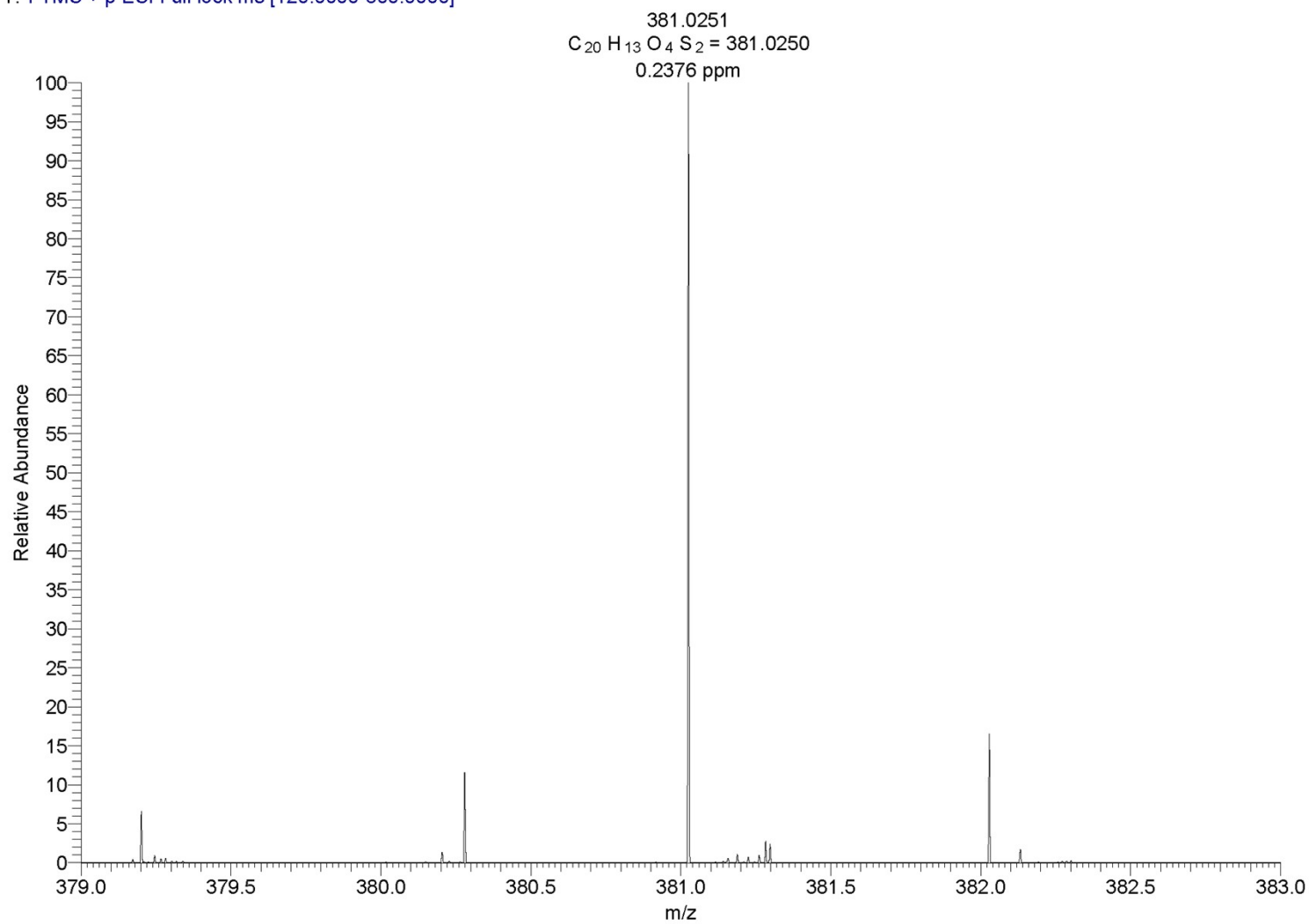
Figure S 7. HRMS ESI mass spectrum of dimethoxy-anthradithiophene quinone
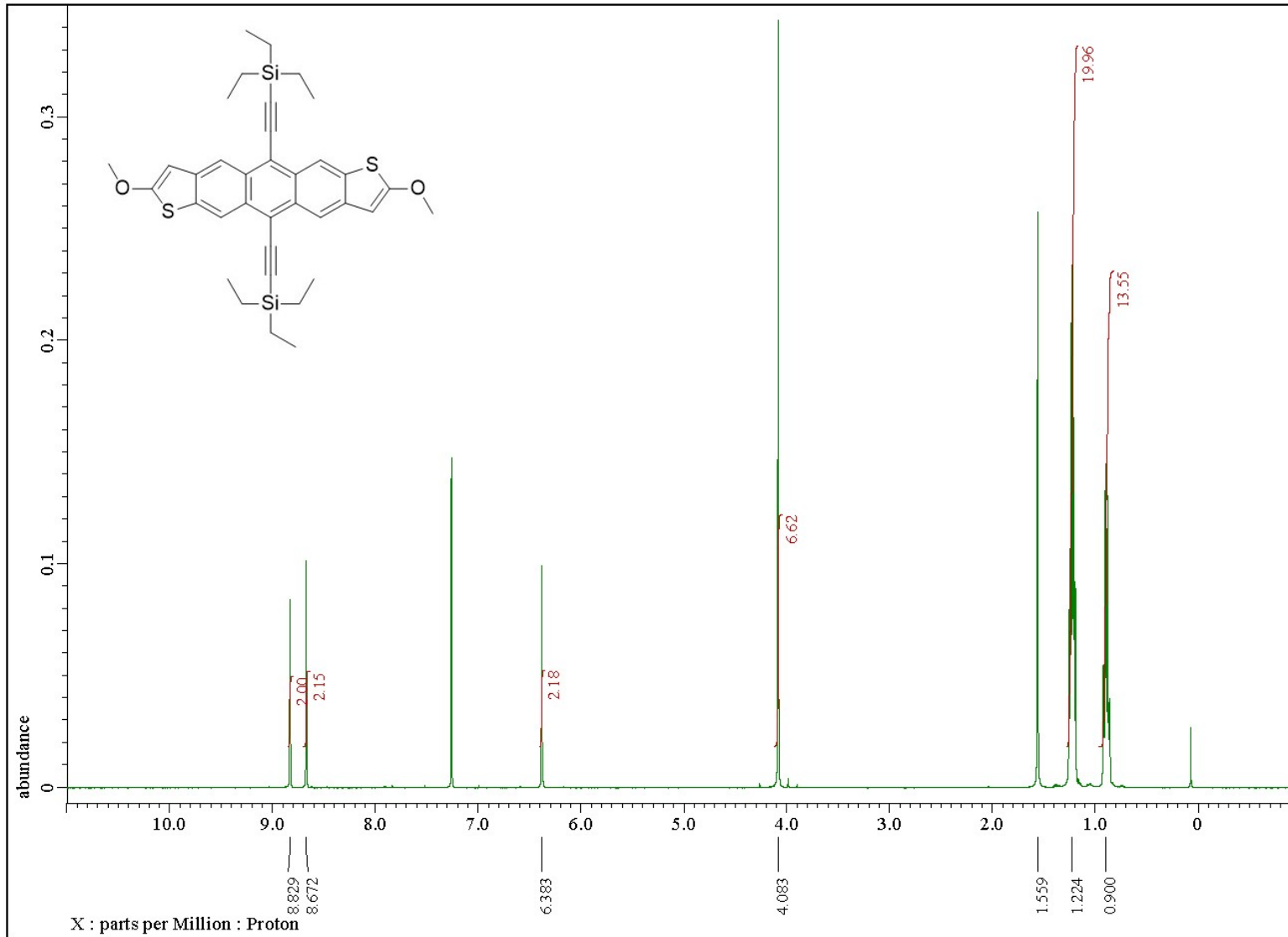
Figure S 8. ^{1}H NMR of triethylsilylethynyl methoxy anthradithiophene measured in CDCl$_3$ at 298 K.
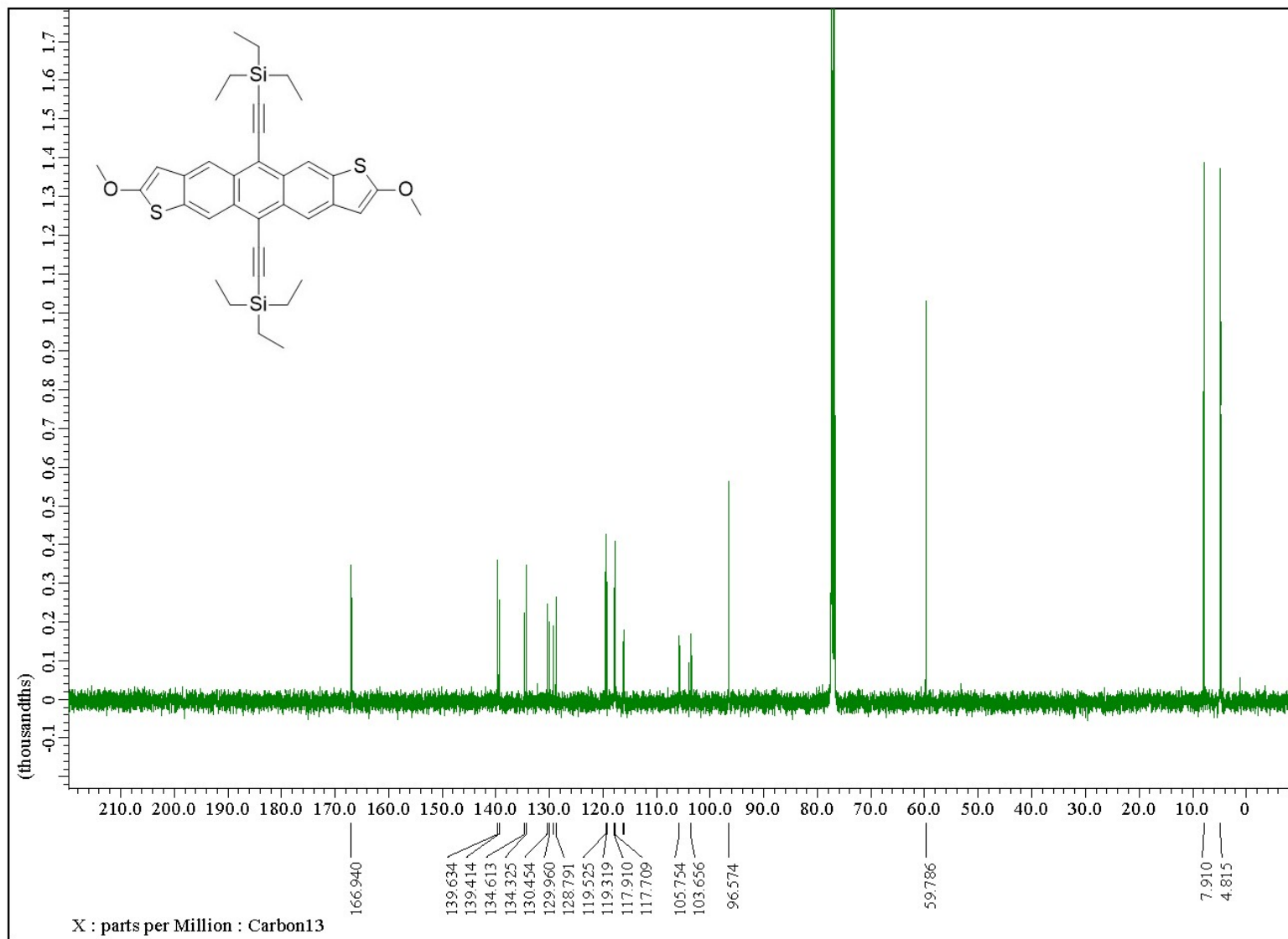
Figure S 9. ^{13}C NMR of triethylsilylethynyl methoxy anthradithiophene measured in CDCl$_3$ at 298 K

OMe-ADT_070122 #44-56   RT: 1.56-1.99   AV: 13   NL: 4.91E5
T: FTMS + p ESI Full lock ms [120.0000-800.0000]
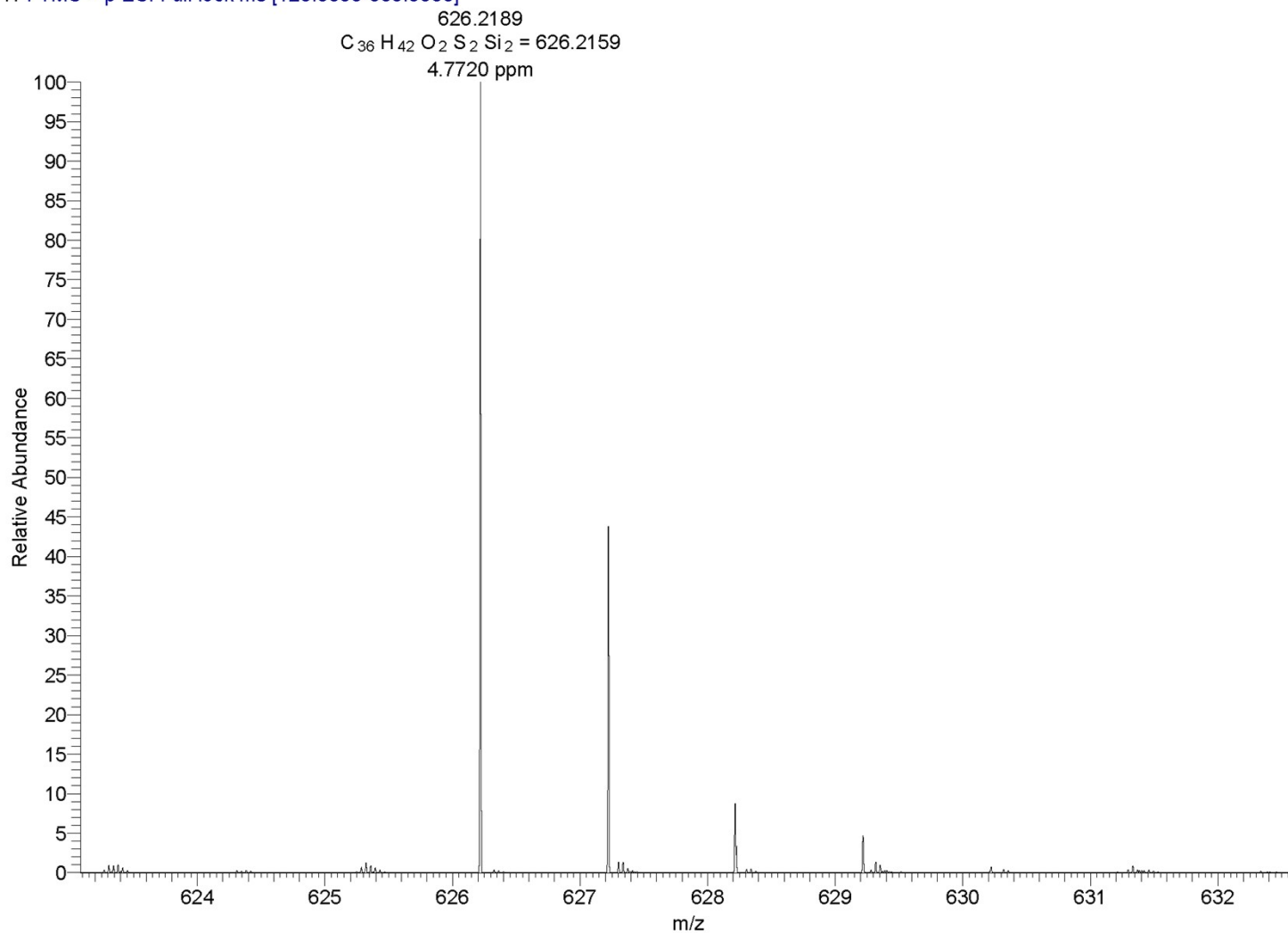
Figure   S   10   HRMS   ESI   mass   spectrum   of   triethylsilylethynyl   methoxy   anthradithiophene

S16

Electrochemistry
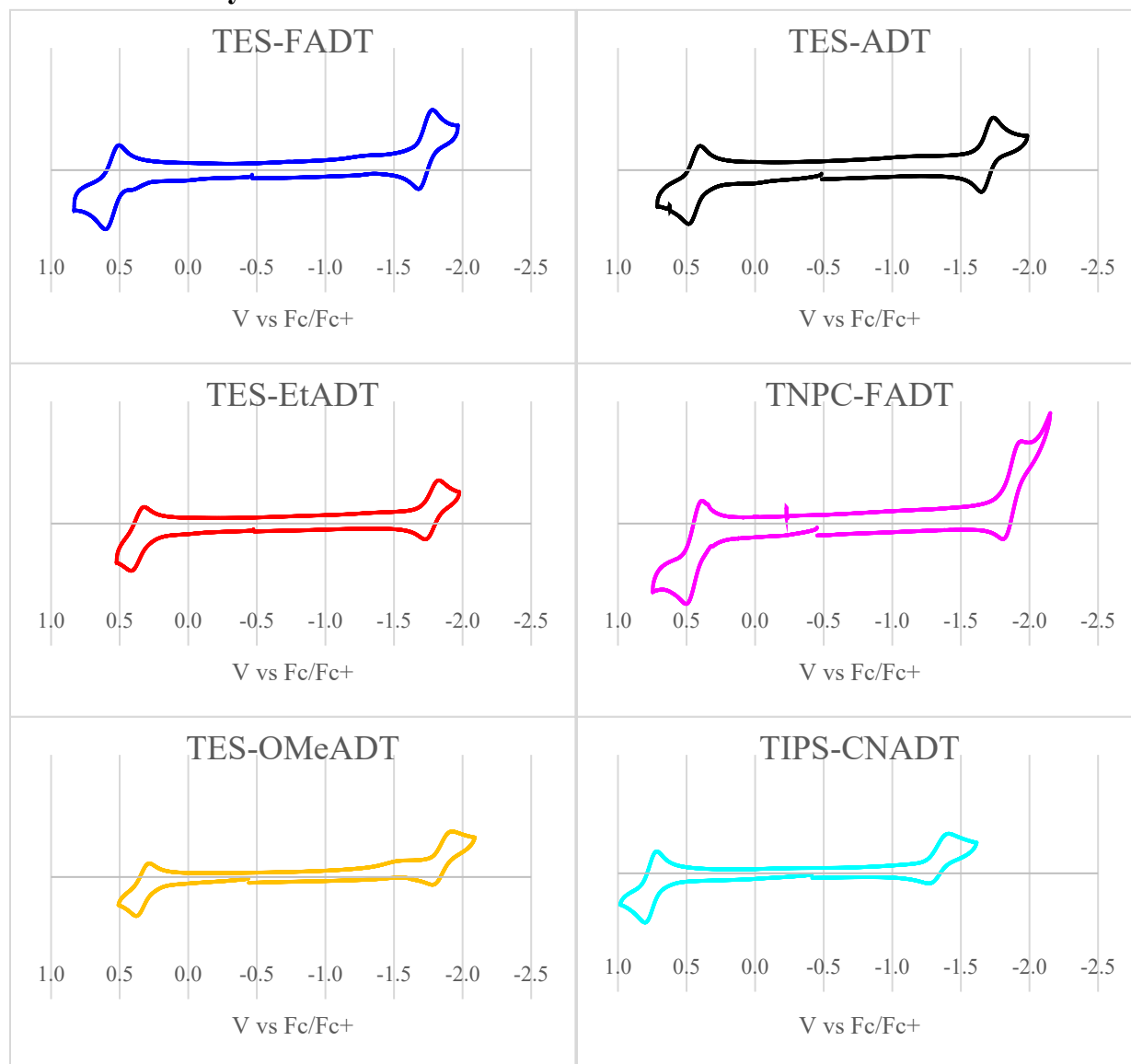
Figure S 11. Cyclic voltammetry traces used to derive approximations to the HOMO and LUMO energies of ADT derivatives, measured in 0.1 M Bu_4NPF_6 in CH_2Cl_2 at 298 K at a scan rate of 50 mV/s. A platinum working electrode, silver counter electrode, and an Ag/AgCl reference electrode were used, and ferrocene (not shown in figure) was added as an internal standard.

UV-Vis Absorption Data
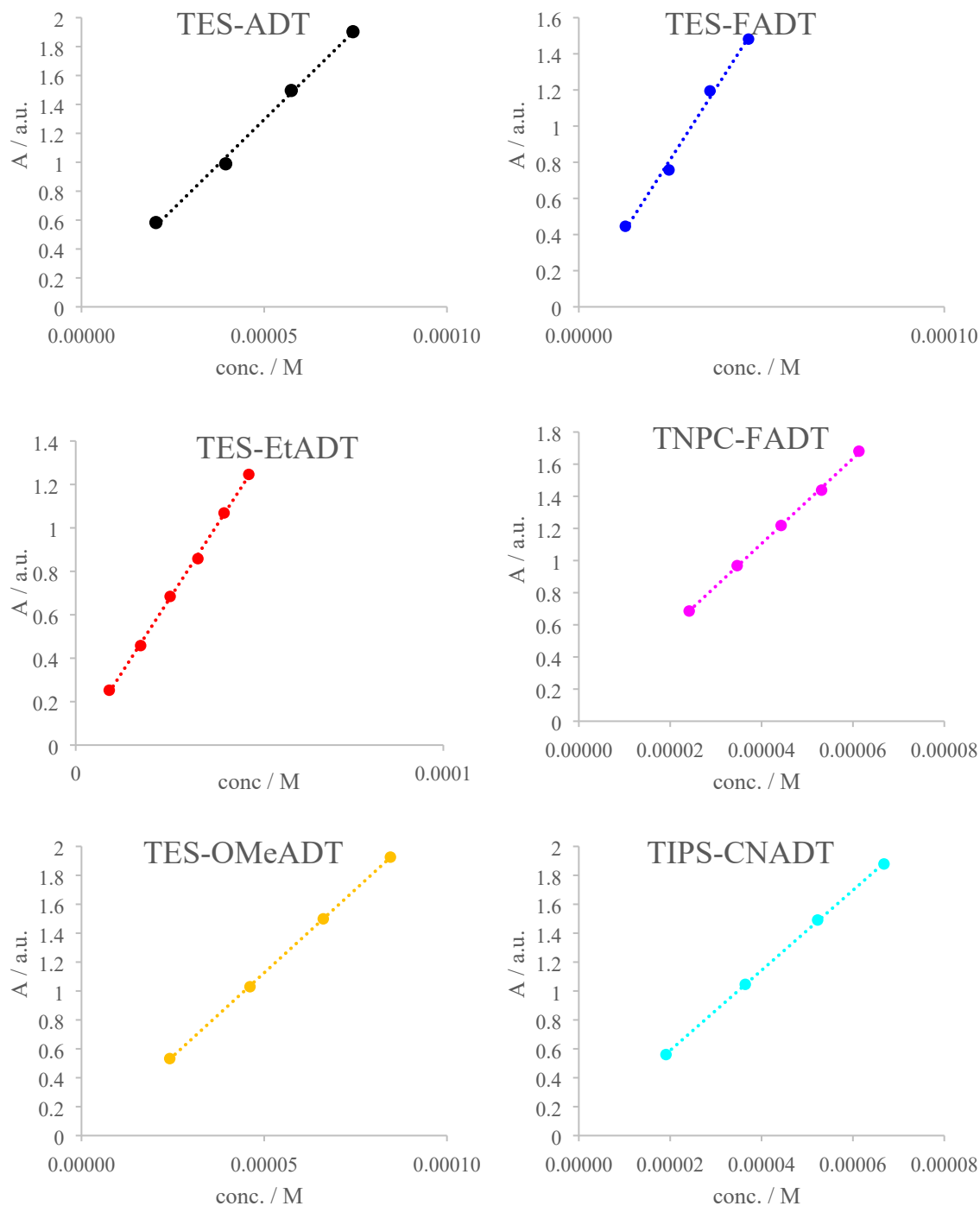
Figure S 12. Plots of absorbance at maxima versus concentration used to determine extinction coefficients for ADT derivatives.
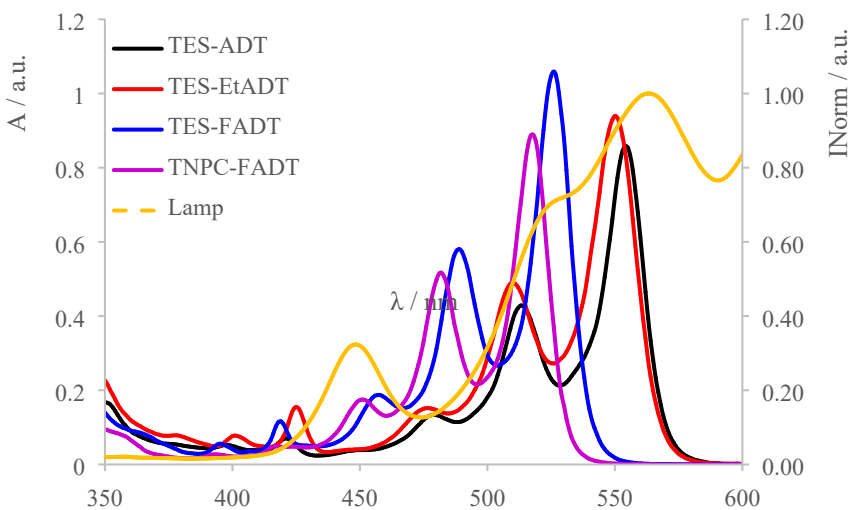
Figure S 13 Absorption spectra of ADT derivatives at 3.3×10⁻⁵ M in CHCl₃ (solid lines) and normalised emission intensity of the LED desk lamp used in this study (dotted line). This corresponds to the data in Figure 2 in the manuscript.
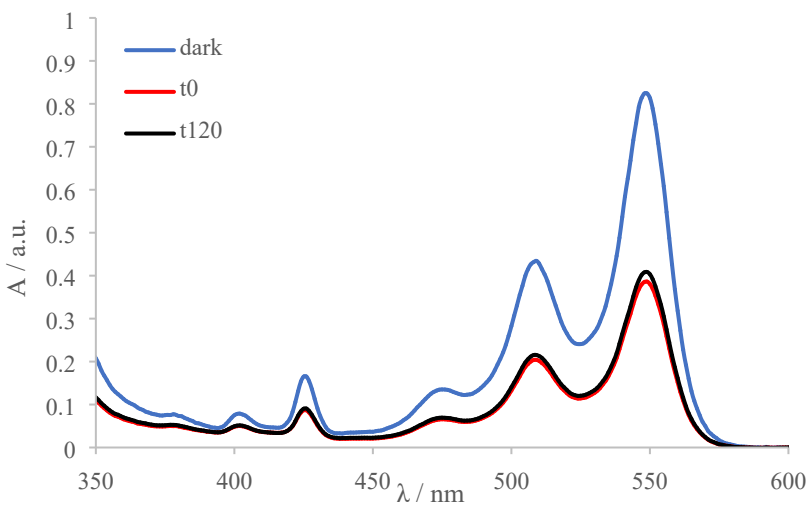
Figure S 14. Example of spectra showing slow thermal reversibility of endoperoxide formation. The blue "dark" line shows the initial spectrum of freshly prepared ADT in CHCl₃ at concentration of 3.3×10⁻⁵ M. This sample was irradiated with white light until the absorptivity was half of the original value (red line). The light was turned off, and spectra were collected every 5 minutes over 2 hours. The final spectrum after two hours is shown in black.
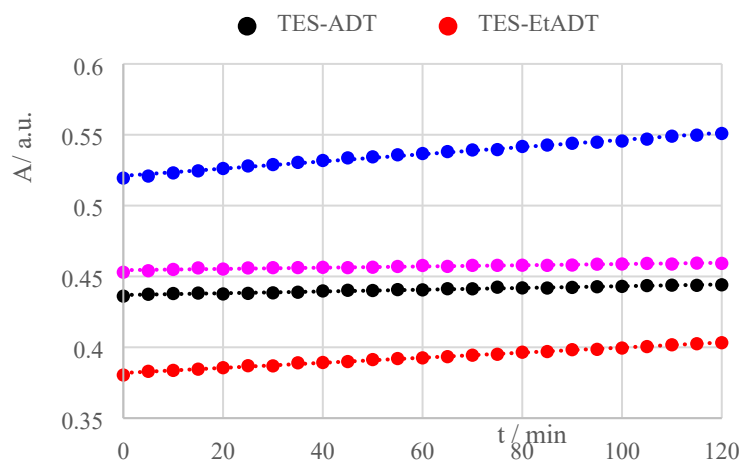
Figure S 15. Thermal reversibility of ADT endoperoxide formation, monitored by the change in absorption at λ_{max} of ADT / endoperoxide mixtures prepared as in Figure S11.

Green LED Excitation
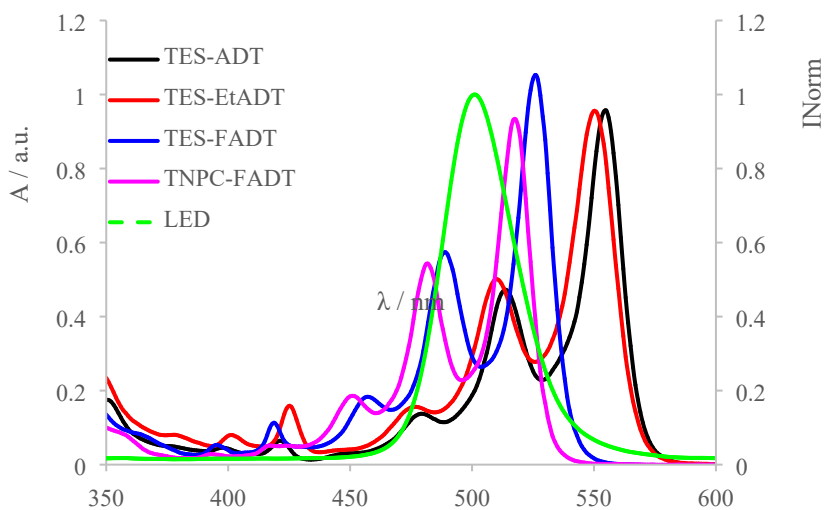
Figure S 16. Absorption spectra of ADT derivatives at 3.3×10^{-5} M in CHCl$_3$ (solid lines) and normalised emission intensity of the green LED used in this study (dotted line)
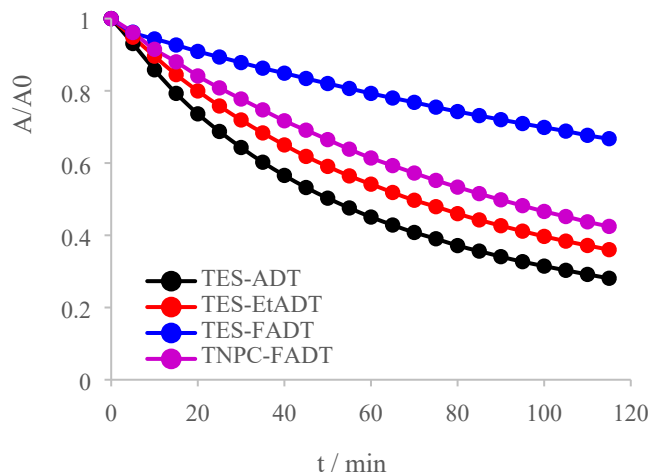
Figure S 17 Relative absorbance over time for ADT derivatives at 3.3×10⁻⁵ M in CHCl₃ irradiated with the green LED.
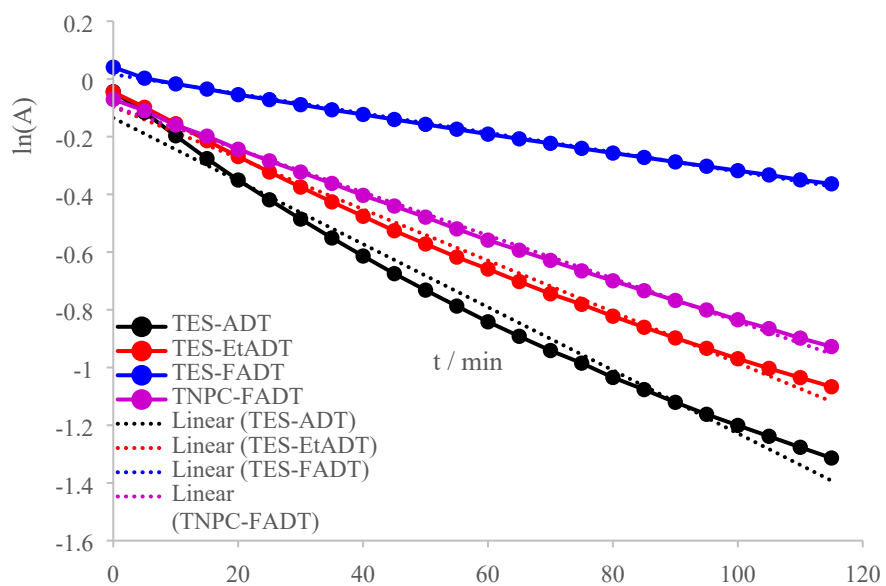
Figure S 18 Fit of photodecomposition of ADTs by green LED to a 1ˢᵗ order reaction by plotting ln(A) versus time.
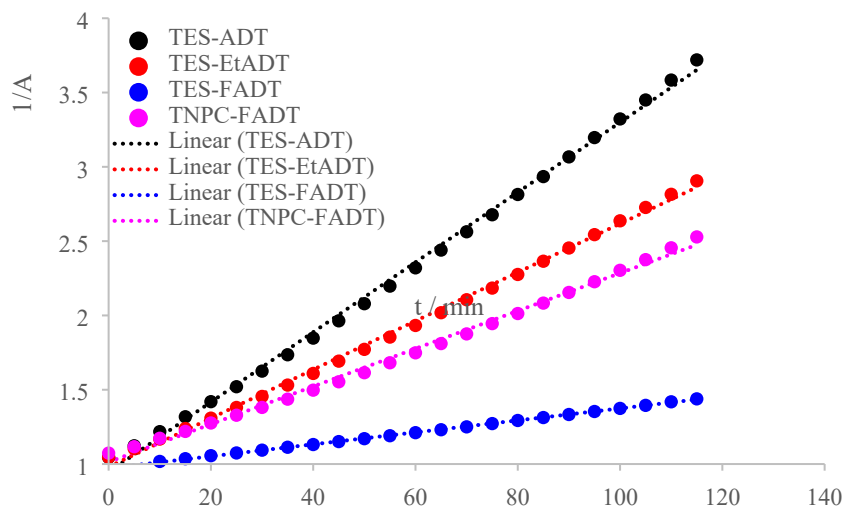
Figure S 19 Fit of photodecomposition of ADTs by green LED to a 2nd order reaction by plotting 1/A versus time.
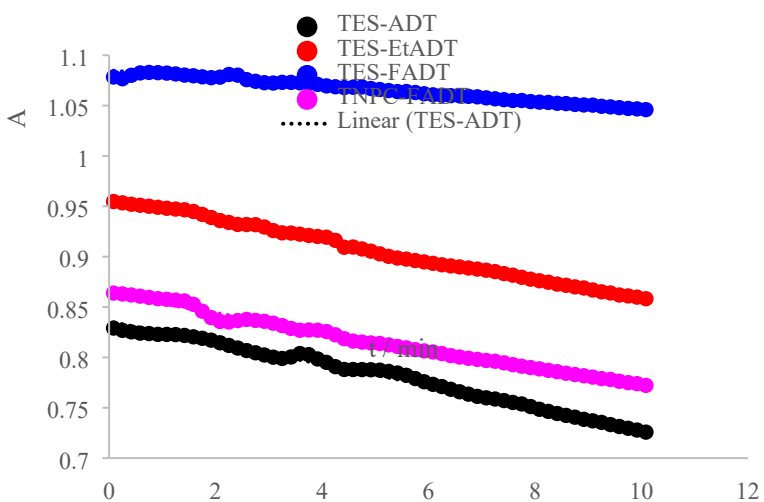
Figure S 20 Linear fit to determine initial rate of reaction for ADTs at 3.3×10^{-5} M in CHCl$_3$ illuminated by the green LED. This data corresponds to Figure 3 in the manuscript.

Blue LED Excitation
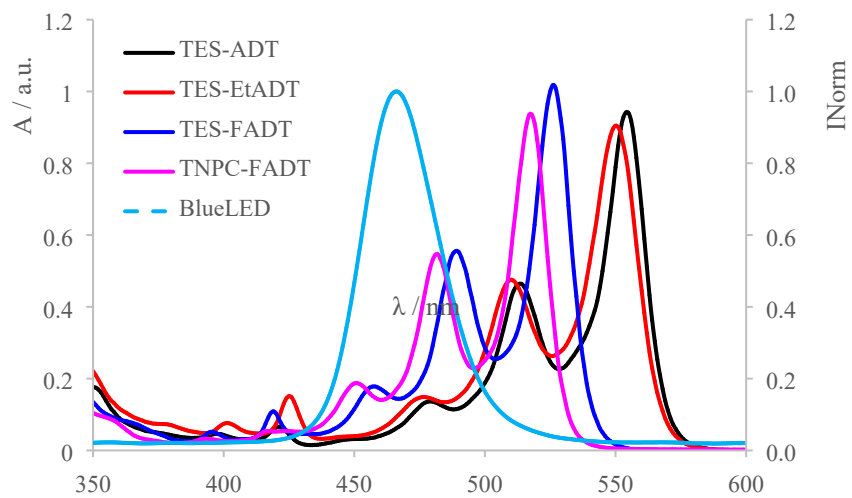
Figure S 21 Absorption spectra of ADT derivatives at 3.3×10⁻⁵ M in CHCl₃ (solid lines) and normalised emission intensity of the blue LED used in this study (dotted line)
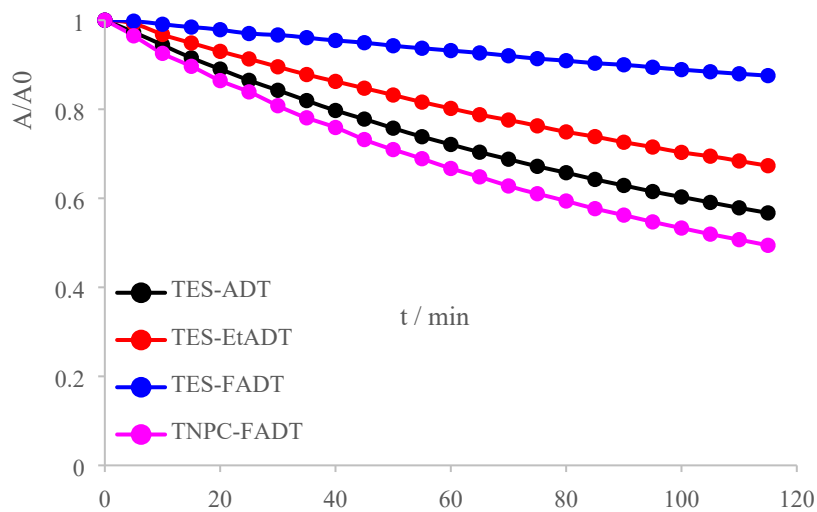
Figure S 22 Relative absorbance over time for ADT derivatives at 3.3×10⁻⁵ M in CHCl₃ irradiated with the blue LED
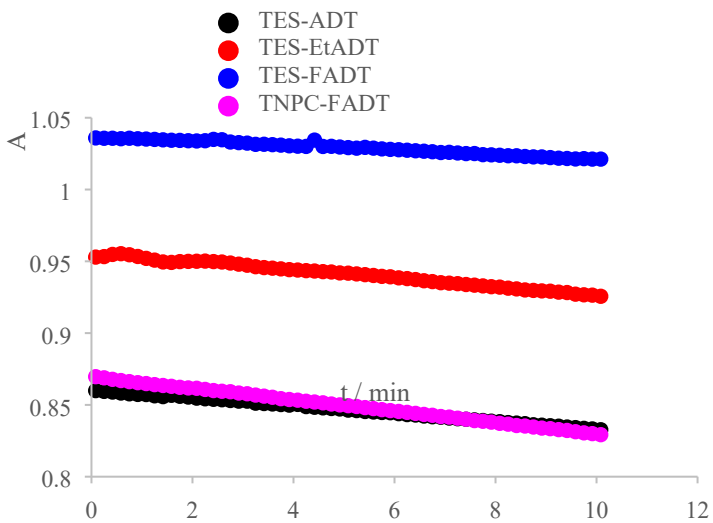
Figure S 23 Linear fit to determine initial rate of reaction for ADTs at 3.3×10⁻⁵ M in CHCl₃ illuminated by the blue LED. This data corresponds to Figure 3 in the manuscript.

White LED Excitation
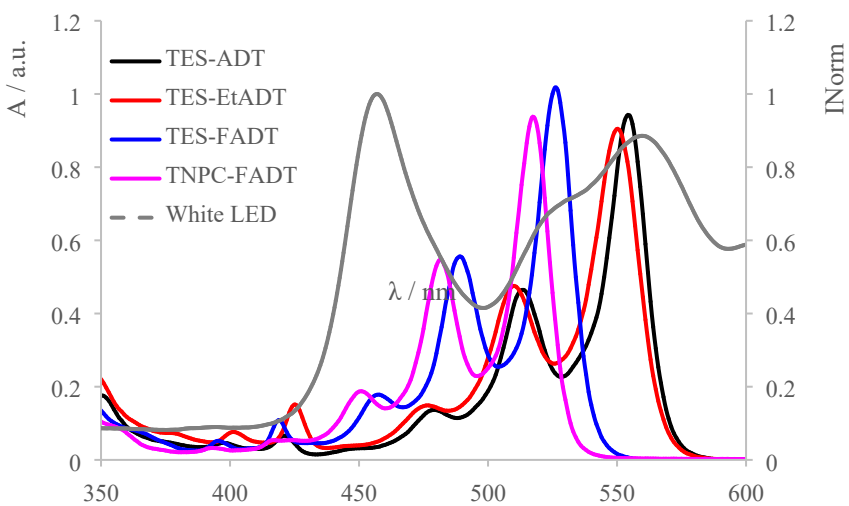
Figure S 24 Absorption spectra of ADT derivatives at 3.3×10⁻⁵ M in CHCl₃ (solid lines) and normalised emission intensity of the white LED used in this study (dotted line)
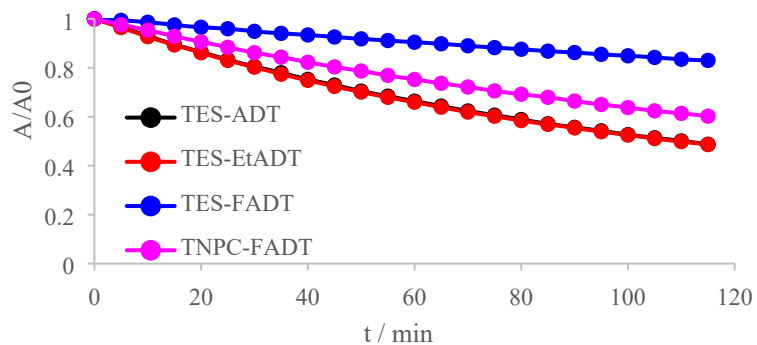
Figure S 25 Relative absorbance over time for ADT derivatives at 3.3×10^{-5} M in CHCl$_3$ irradiated with the white LED.
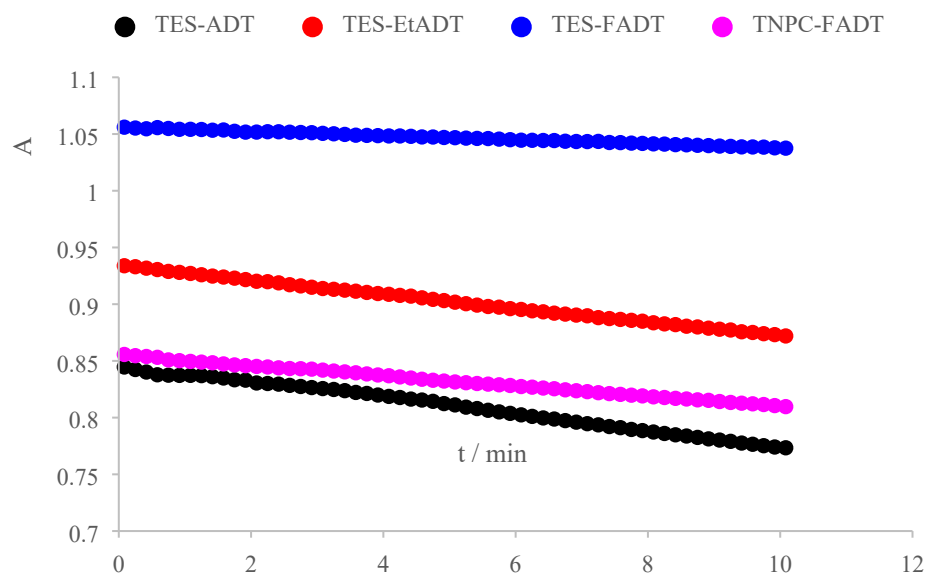
Figure S 26 Linear fit to determine initial rate of reaction for ADTs at 3.3×10^{-5} M in CHCl$_3$ illuminated by the white LED. This data corresponds to Figure 3 in the manuscript.

Concentration Dependence
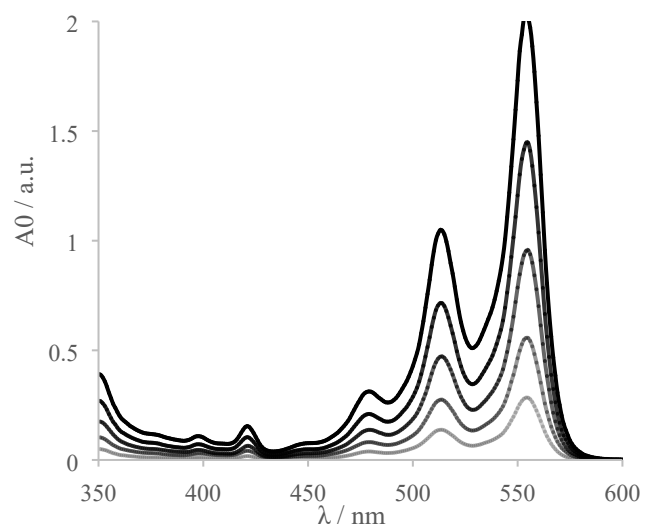
Figure S 27. Initial absorption spectra of TES-ADT at different concentrations used in concentration dependence studies, see Figure 4 of the main text.
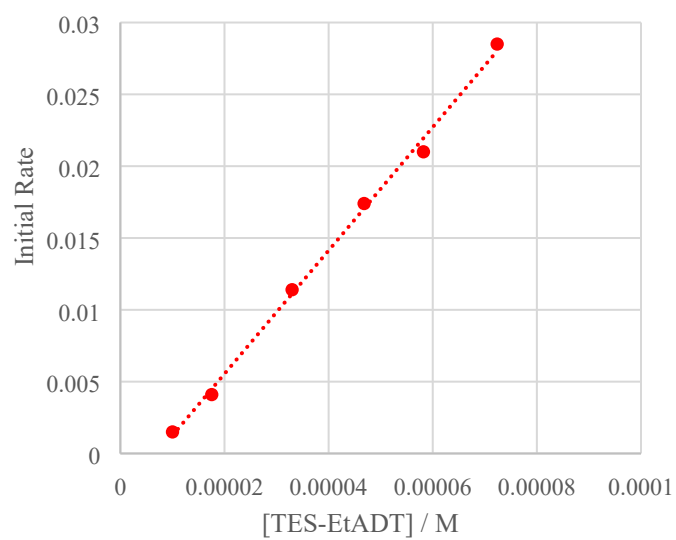
Figure S 28. Concentration dependence of rate of TES-EtADT photooxidation in CHCl$_3$ at 298 K under illumination by green LED.
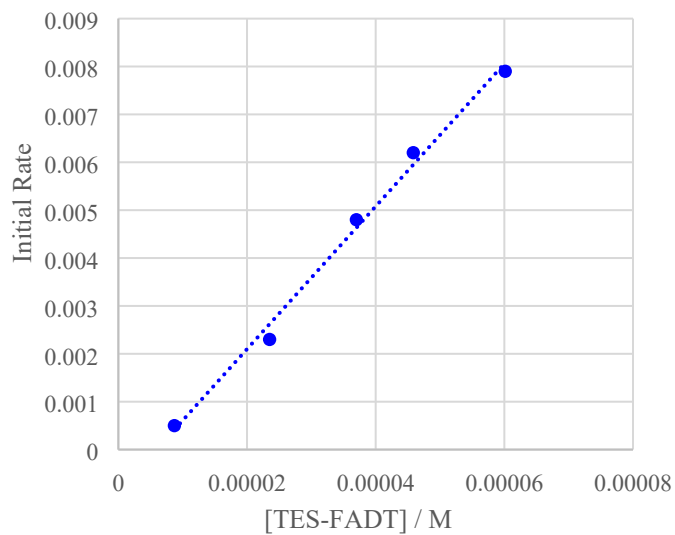
Figure S 29. Concentration dependence of rate of TES-FADT photooxidation in CHCl$_3$ at 298 K under illumination by green LED.
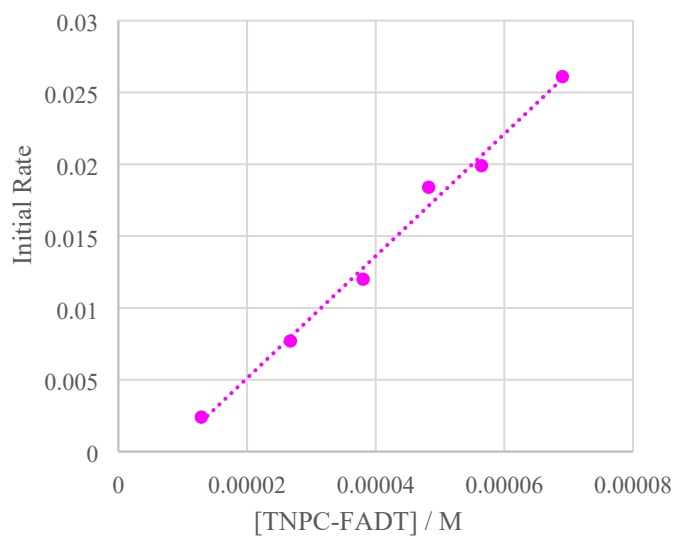
Figure S 30. Concentration dependence of rate of TNPC-FADT photooxidation in CHCl$_3$ at 298 K under illumination by green LED.

Solvent Effects
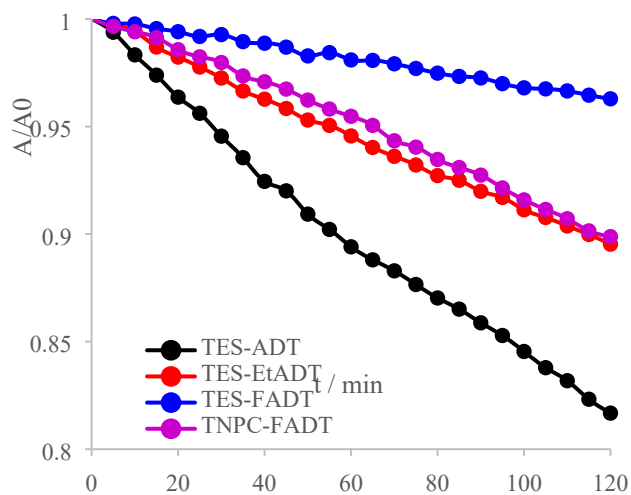
Figure S 31. Relative absorbance over time ADT derivatives at 3.3×10⁻⁵ M in toluene under irradiation with the green LED.
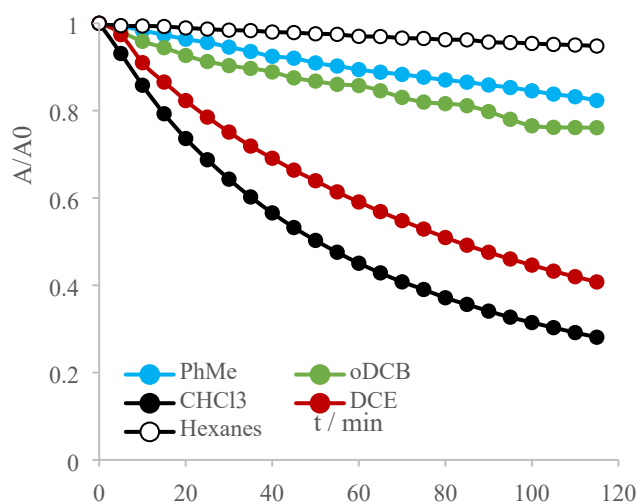
Figure S 32. Relative absorbance over time TES-ADT at 3.3×10⁻⁵ M in different solvents under irradiation with the green LED.
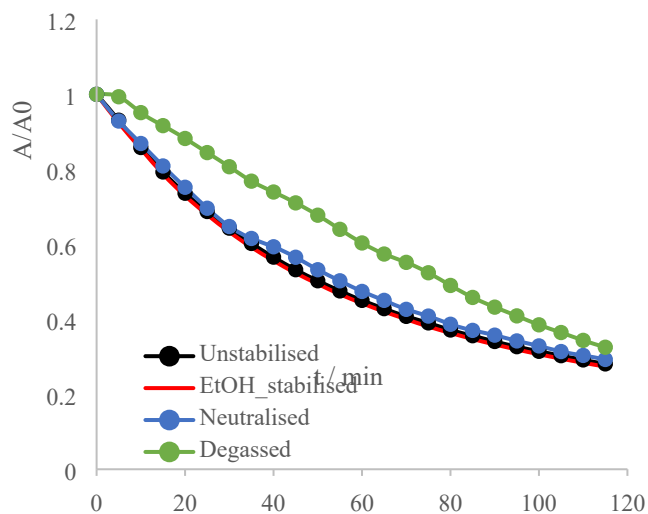
Figure S 33. Relative absorbance over time TES-ADT at 3.3×10^{-5} M in different chloroform sources. Neutralised CHCl$_3$ was prepared by stirring with K$_2$CO$_3$ for one hour, removing the solid by filtration before measurement. Degassed solvent was prepared by bubbling with argon for 90 minutes before measurement, although a gas-tight fit of the cuvette was not possible with our current experimental setup.
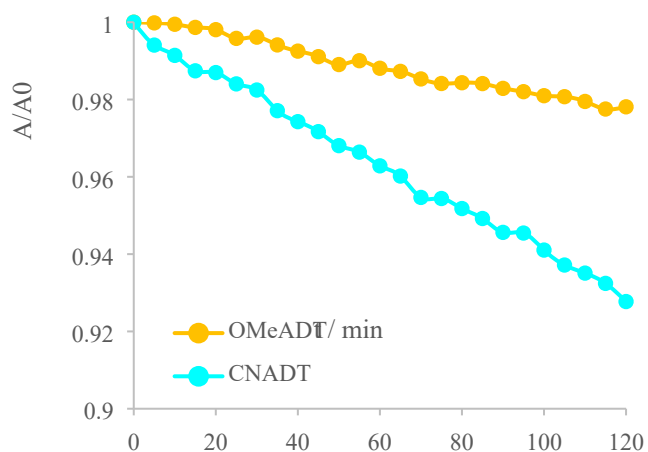
Figure S 34. Relative absorbance over time for methoxy and nitrile ADT derivatives at 3.3×10^{-5} M in toluene irradiated with the white LED.

Methylene Blue Sensitization
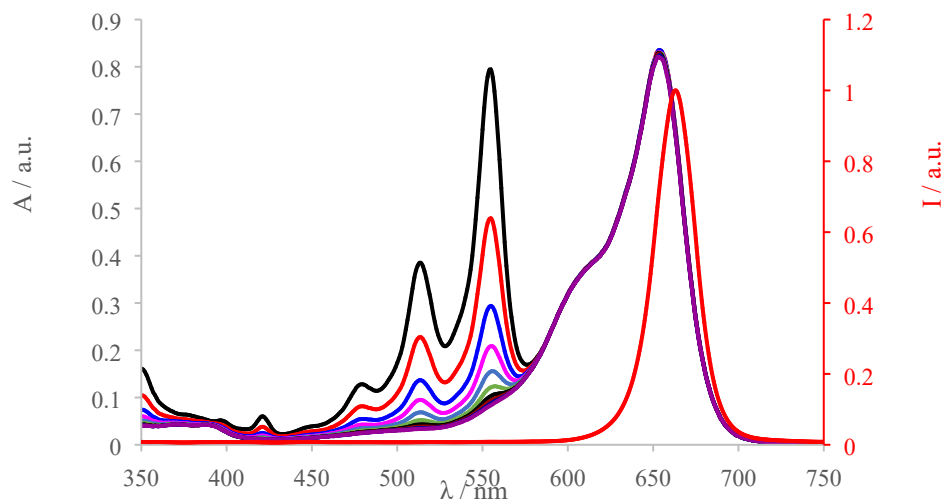
Figure S 35 Absorption spectra (solid lines) of a mixture of TES-ADT at 3.3×10^{-5} M in CHCl$_3$ (peaks between 450 and 550 nm) and methylene blue (peak at 650 nm and shoulder at 600 nm) at timed intervals over 2 hours under red LED illumination. Normalised emission intensity of the red LED is shown as the red dotted line.
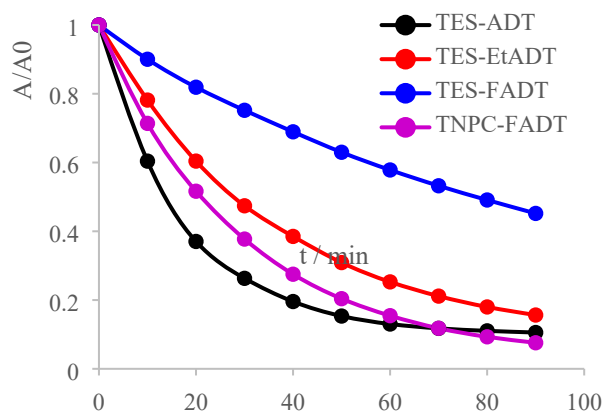
Figure S 36 Relative absorbance of ADT derivatives at 3.3×10^{-5} M in CHCl$_3$ over time when a mixture of ADT and methylene blue were irradiated with the red LED
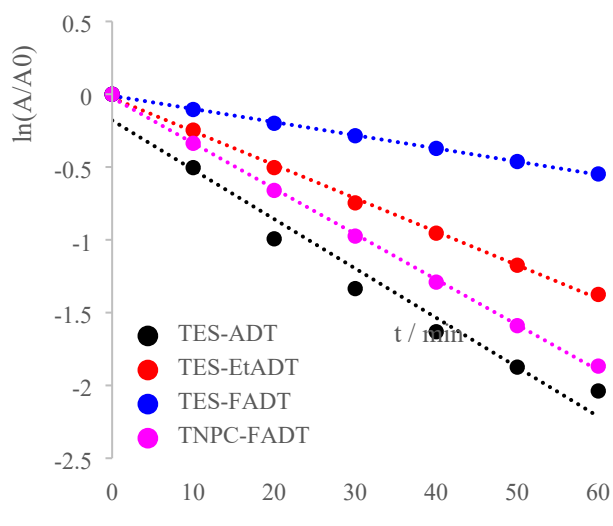
Figure S 37. 1st order fitting of data from Figure S32
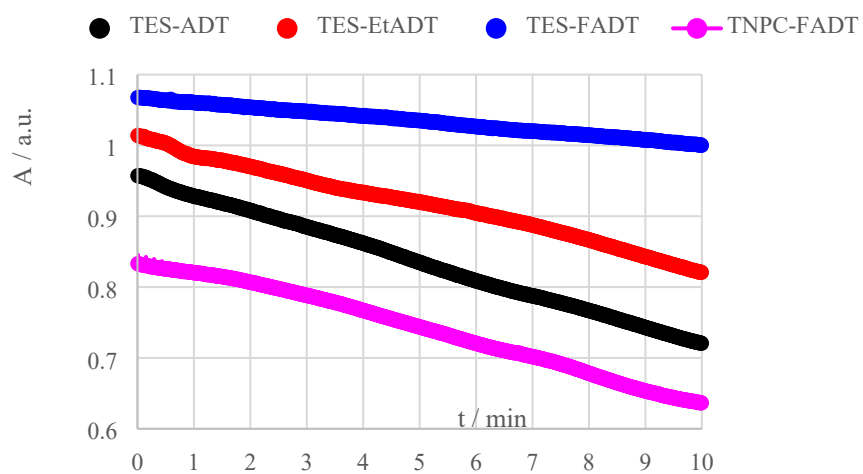
Figure S 38. Linear fit to determine initial rate of reaction for ADTs at 3.3×10^{-5} M in CHCl$_3$ with the same amount of methylene blue, illuminated by the red LED. This data corresponds to data in Figure 6 in the manuscript.
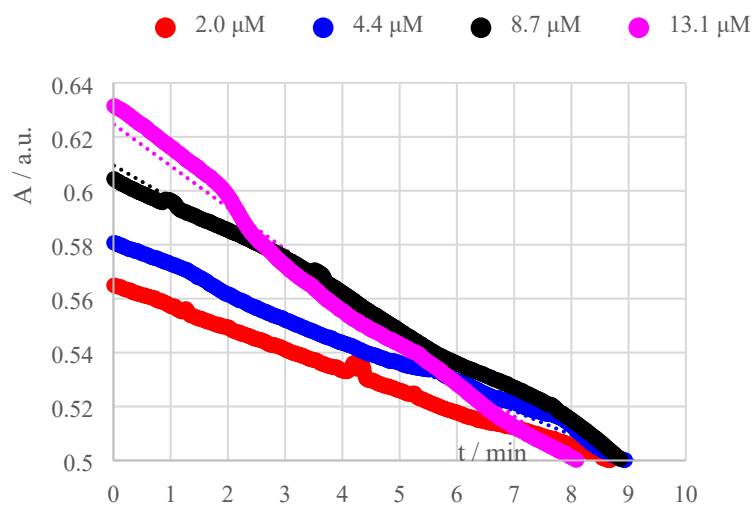
Figure S 39. Linear fit to determine initial rate of reaction for TES-ADT at 3.3×10^{-5} M in $CHCl_3$ with different concentrations of methylene blue, illuminated by the red LED.
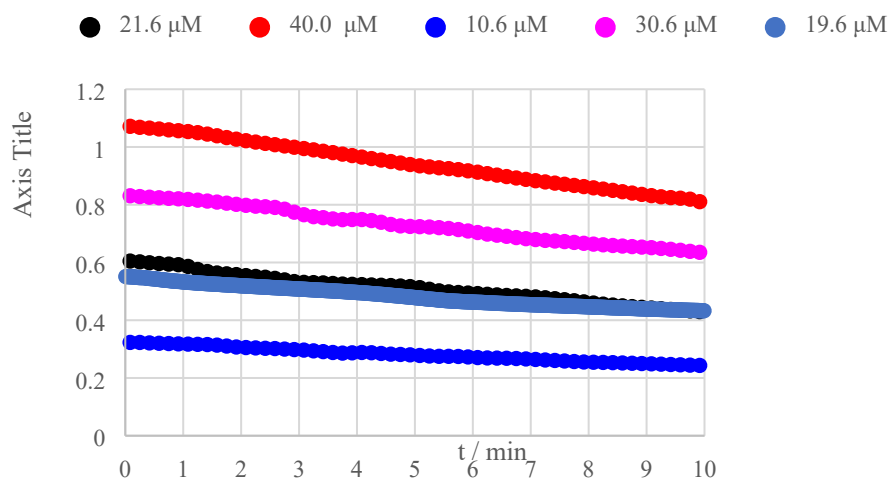
Figure S 40. Linear fit to determine initial rate of reaction for TES-ADT at different concentrations in $CHCl_3$ with constant concentration of methylene blue, illuminated by the red LED.
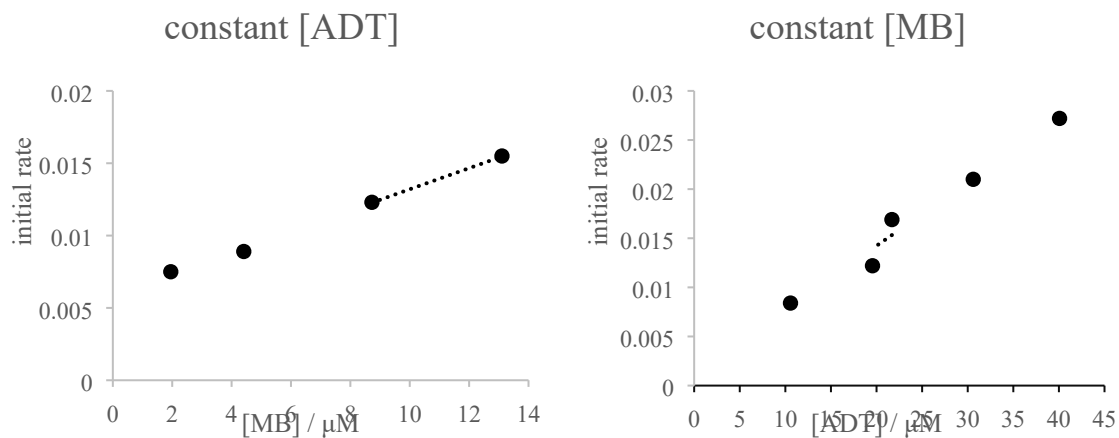
Figure S 41. Concentration dependence of photosensitised oxidation of TES-ADT using methylene blue. (Left) constant TES-ADT concentration and (right) constant methylene blue concentration.

Additional NMR data
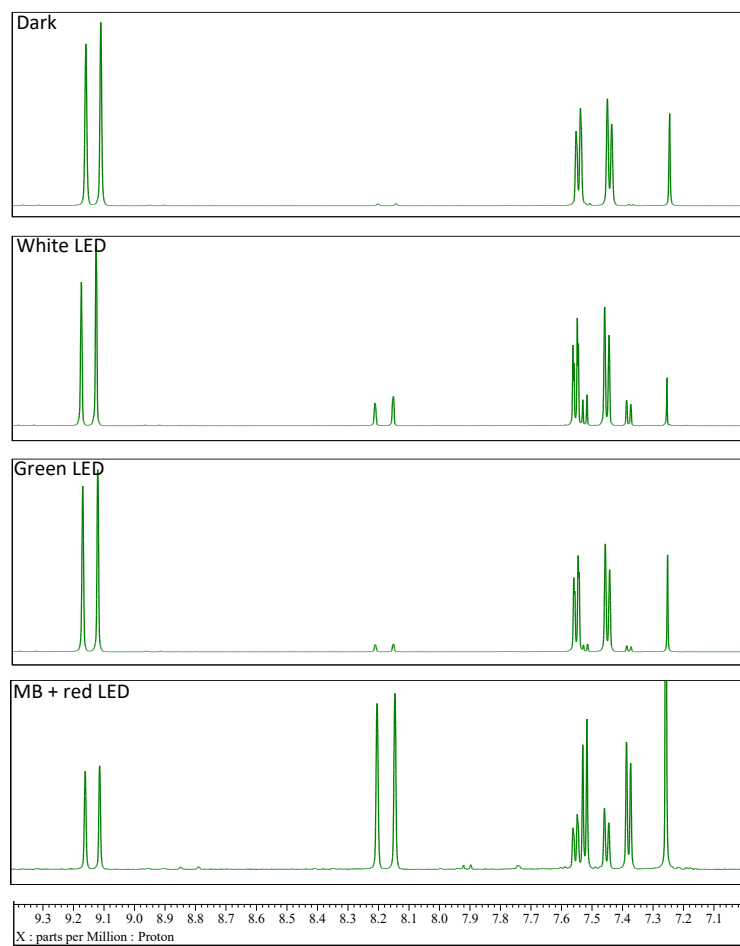
Figure S 42. Aromatic region of the ^{1}H NMR spectra of TES-ADT in the dark, and after illumination by different light sources for 3 hours or with addition of methylene blue. All spectra recorded in CDCl₃ at 298 K.
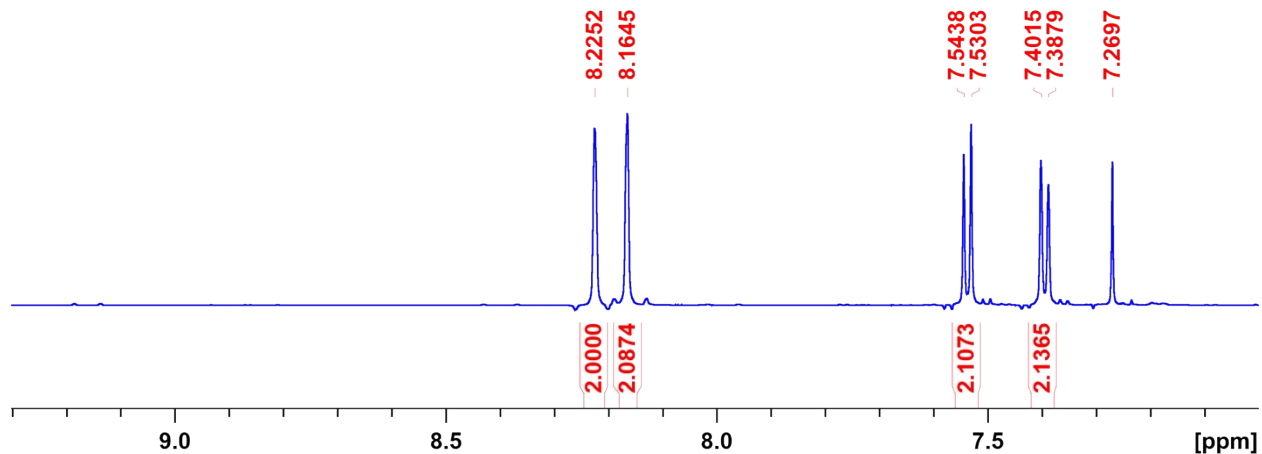
Figure S 43. Aromatic region of the ^{1}H NMR spectra of TES-ADT photoproduct formed in toluene by illumination by LED desklamp for 8 hours. The solvent was removed and the material redissolved in CDCl$_3$ for NMR measurement.
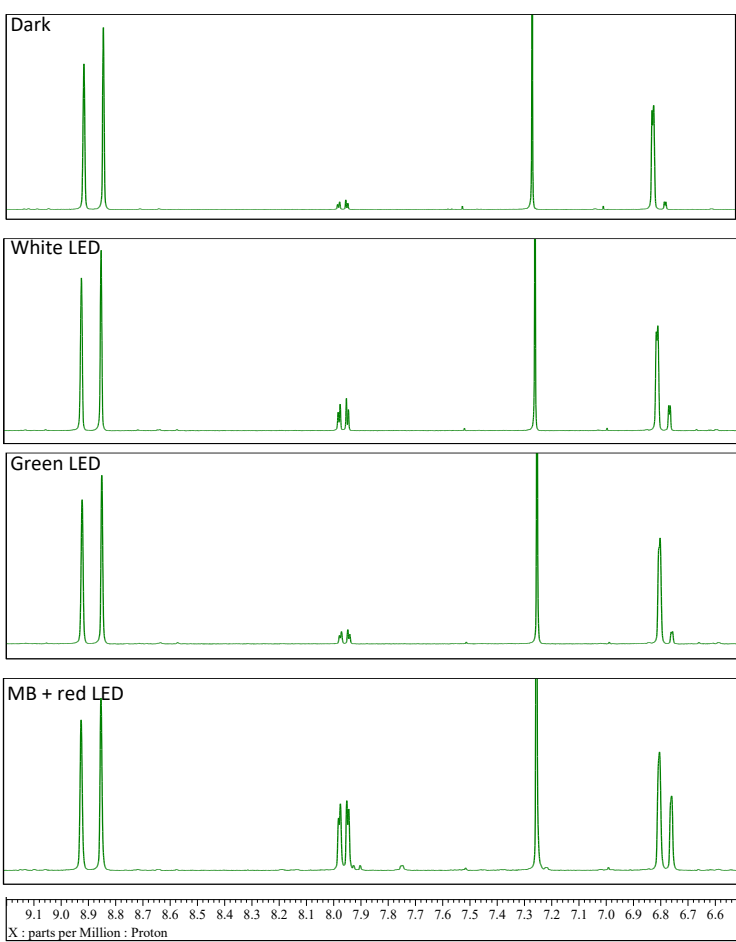
Figure S 44. Aromatic region of the ^{1}H NMR spectra of TES-FADT in the dark, and after illumination by different light sources for 3 hours or with addition of methylene blue. All spectra recorded in CDCl$_3$ at 298 K.
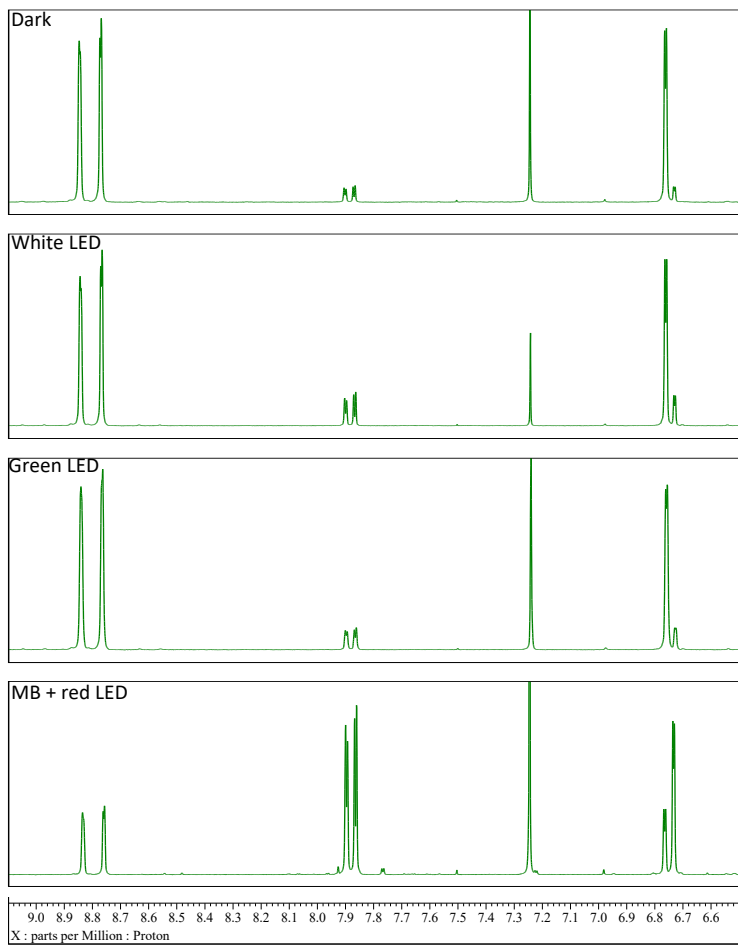
Figure S 45. Aromatic region of the ^{1}H NMR spectra of TNPC-FADT in the dark, and after illumination by different light sources for 3 hours or with addition of methylene blue. All spectra recorded in CDCl$_3$ at 298 K.
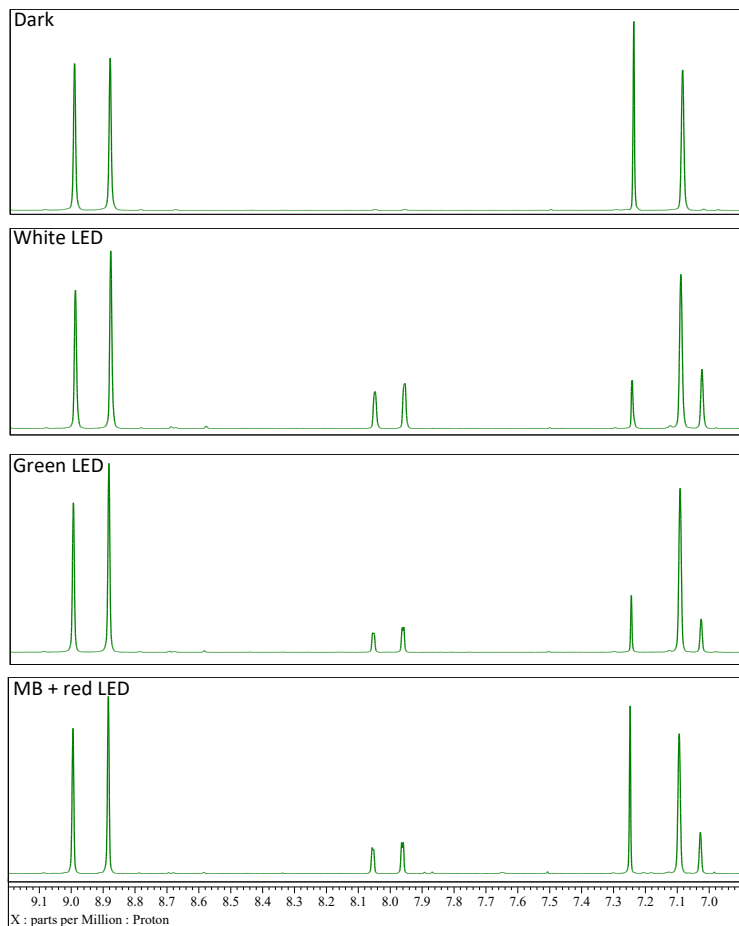
*Figure S 46*Aromatic region of the ^{1}H NMR spectra of TES-EtADT in the dark, and after illumination by different light sources for 3 hours or with addition of methylene blue. All spectra recorded in CDCl$_3$ at 298 K
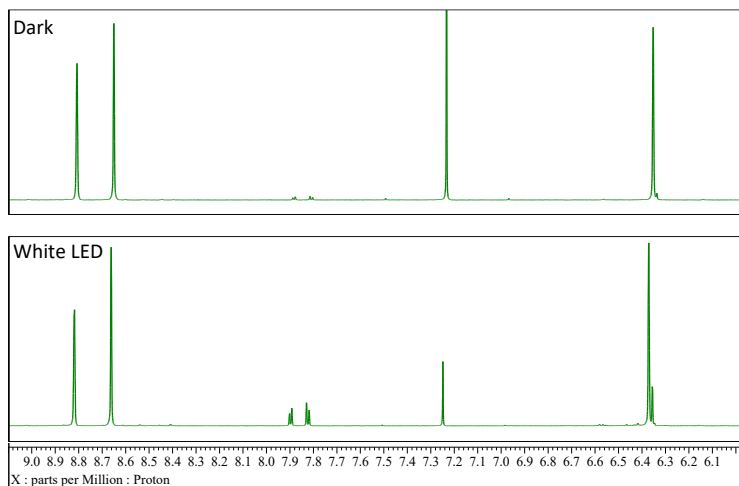
Figure S 47. Aromatic region of the ^{1}H NMR spectra of TES-OMeADT in the dark, and after illumination by white LED for 3 hours. Spectra recorded in CDCl$_3$ at 298 K.
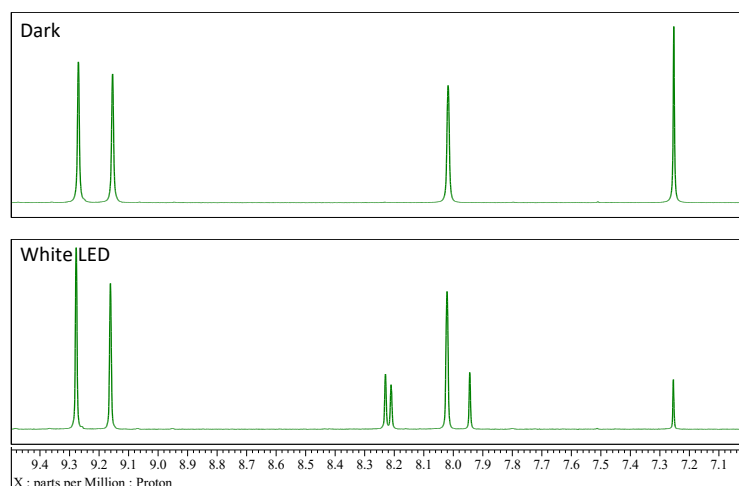
Figure S 48. Aromatic region of the ^{1}H NMR spectra of TIPS-CNADT in the dark, and after illumination by white LED for 3 hours Spectra recorded in CDCl$_3$ at 298 K.

Computational Details

Molecular Properties

Table S 1. Molecular properties calculated using optimally tuned ωB97XD/6-31G* in CHCl$_3$ polarisable continuum. Redox properties were calculated as the difference in total energies of different oxidation states at the neutral optimised geometry. The lowest energy excitations were calculated using TD-DFT and oscillator strengths, *f*, were taken from these calculations. Transition dipole moments, μ_{ag}, were derived from the experimental extinction coefficient vs wavenumber plot by integration over the S0-S1 absorption band (16 700 to 23 000 cm^{-1}). Half-width at half-maximum (HWHM) values were measured on the low energy side of the first vibronic peak.

	IP / eV	EA / eV	E$_{exc}$ / eV	*f*	μ_{ag} / D	HWHM / cm^{-1}
TES-ADT	5.13	2.38	2.23	0.3506	2.1	224
TES-FADT	5.24	2.37	2.36	0.3712	2.3	286
TES-EtADT	5.05	2.28	2.25	0.3396	2.3	294
TNPC-FADT	5.09	2.16	2.39	0.3481	2.0	257

Reaction Path Calculation

Reaction paths were calculated using Gaussian by running a series of constrained geometry calculations (opt=modredundant) with fixed C-O bond lengths at the centre ring of the ADT and interacting singlet oxygen molecule (blue arrows in Figure S44). Starting from a molecular mechanics optimized endoperoxide structure, this bond length was increased from 1.2 up to 3 Å in steps of 0.1 Å. Once the scan was complete, the same procedure was applied to the area around the transition state with steps of 0.01 Å for 0.1 Å in either direction from the maximum. Geometries at the two energetic minima (ADT-^{1}O$_2$ complex and ADT-endoperoxide) were optimized without constraints, and confirmed as stationary points by frequency analysis. These optimized geometries, along with the geometry with highest energy around the transition state, were used in a transition state search (opt=qst3) which yielded true transition states in some, but not all, cases. Transition states were characterized by a single imaginary frequency around -300 cm^{-1}, which corresponds to the C-O bond stretching (Figure S46). All calculations were carried out using M06-2X/cc-pVDZ in the gas phase.
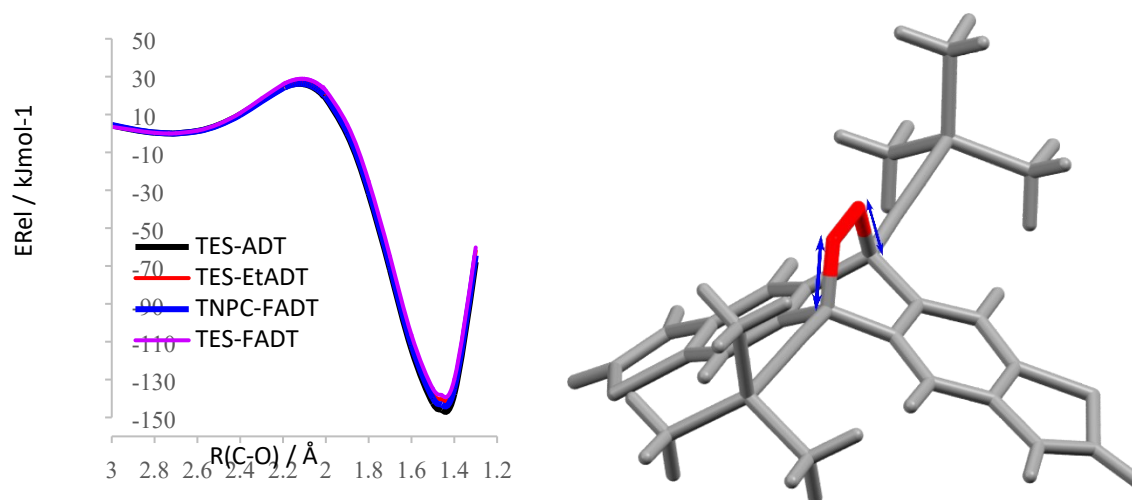
Figure S 49. Computed reaction paths for endoperoxide formation of ADT derivatives, calculated by optimising structures with varying carbon-oxygen bond lengths shown as blue arrows. Energies are relative to the respective ADT-$^1O_2$ van der Waals' complexes signified by the energetic minima with R(C-O) approximately 2.7 Å.
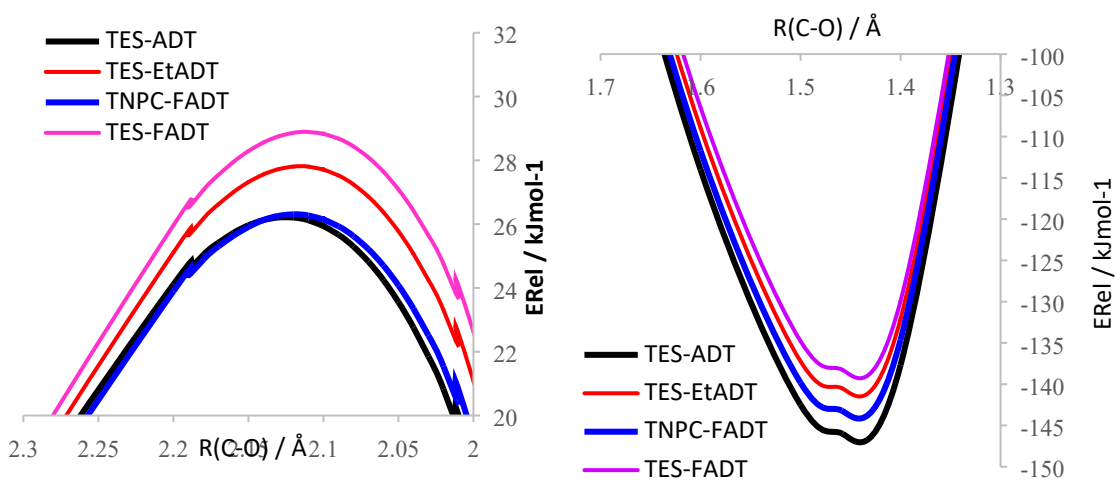
Figure S 50. Zoomed plots of (left) transition state and (right) endoperoxide regions of the reaction paths for endoperoxide formation of ADT derivatives, calculated by optimising structures with varying carbon-oxygen bond lengths. Energies are relative to the respective ADT-$^1O_2$ van der Waals' complexes signified by the energetic minima with R(C-O) approximately 2.7 Å.
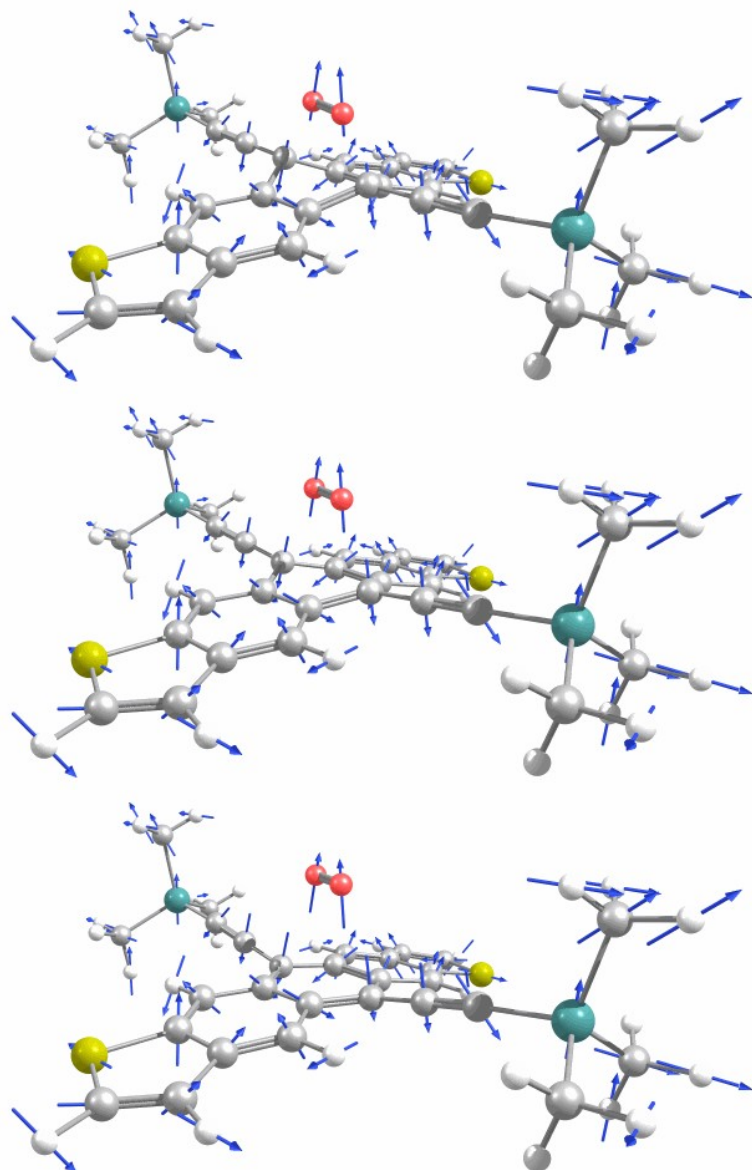
Figure S 51. Normal mode analysis of the TES-ADT-$^1O_2$ transition state imaginary frequency at -300 cm^{-1}, showing (top) negative, (middle) zero, and (bottom) positive displacement corresponding to the C-O bond stretching and resulting ADT atom displacement.

Computational Screening

A range of ADT derivatives were screened for molecular properties to identify potentially interesting materials to test our findings from the initial four ADT molecules. For each molecule, we first optimized the geometry using ωB97XD/6-31G* in CHCl$_3$ polarisable continuum using an ω value of 0.1 which is typical for acenes. Next the functional was tuned (in the gas phase) to best satisfy Koopmans' theorem as described elsewhere,[9] yielding an optimal ω value for each molecule. Next the properties were calculated using a polarizable continuum for CHCl$_3$. Ionization potentials and electron affinities were calculated as energy differences between different electronic states without atomic position relaxation (vertical energies) and reported here as negative numbers in comparison to discussion of HOMO and LUMO energies. Vertical excitation energies were calculated using TD-DFT, with triplet excitations using the Tamm-Dancoff approximation. Relaxed triplet energies were also calculated by comparing single point energies of

geometrically relaxed singlet and triplet states. Reaction energies for screening were calculated by optimizing geometries of ADT and ADT-peroxide in the gas phase, and subtracting energies of ADT and singlet oxygen from the endoperoxide. M06-2X/cc-pVTZ was used in analogy to the reaction path calculations, also avoiding issues with choosing the "correct" range separation parameters when using ωB97XD. Chemical structures differ by the substituent at the thiophene 2 position, and the TES versus TNPC alkynyl side chain.
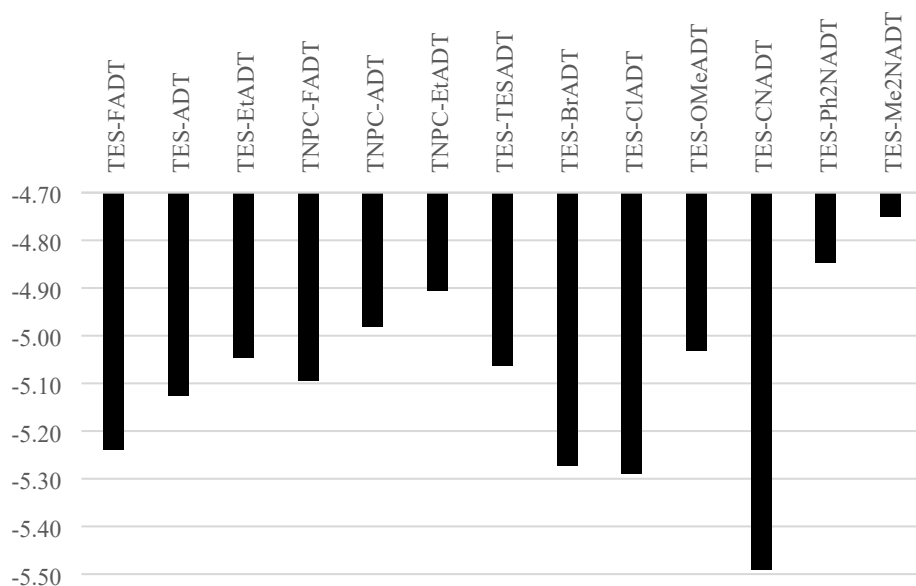
Figure S 52. Computed negative ionisation potentials of a range of ADT derivatives.
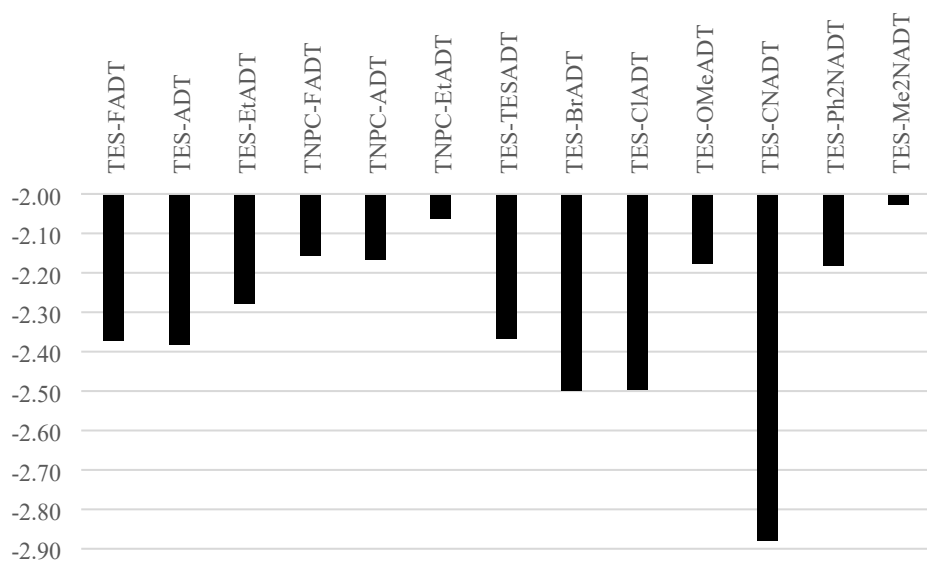
Figure S 53. Computed negative electron affinities of a range of ADT derivatives.
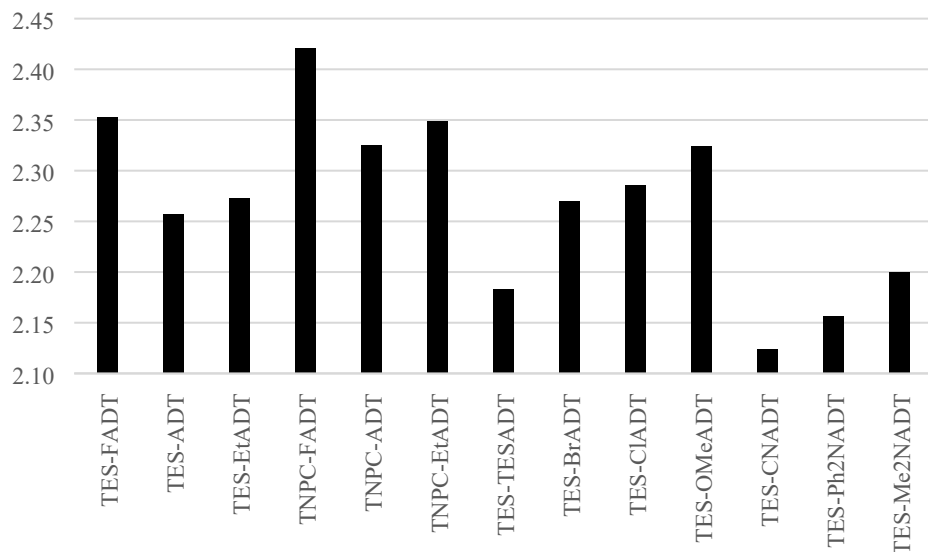
Figure S 54. Computed vertical excitation energies to lowest excited singlet state of a range of ADT derivatives.
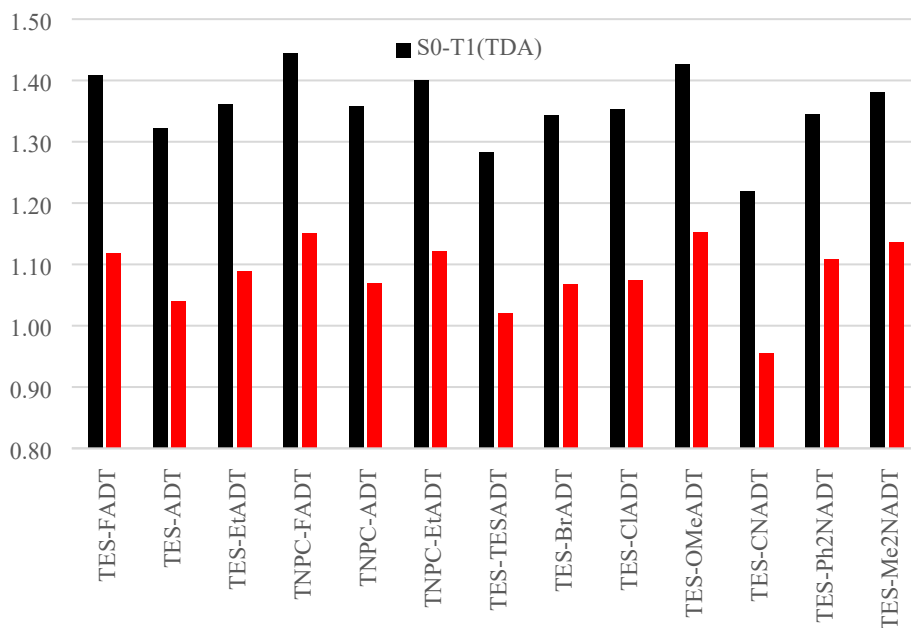
Figure S 55. Computed triplet energies for a range of ADT derivatives, calculated by vertical excitation using the Tamm-Dancoff approximation (black bars) and by difference in single point energies of relaxed structures in singlet and triplet states (red bars).
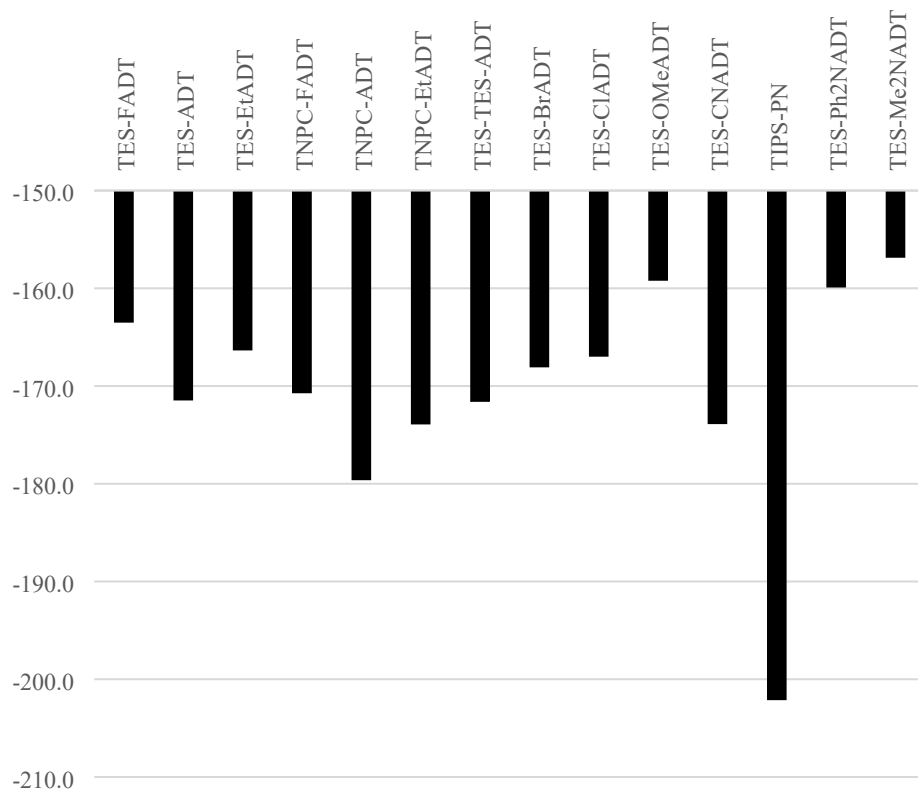
Figure S 56. Computed reaction energies for a range of alkynyl ADT derivatives undergoing reaction with singlet oxygen to yield endoperoxides. TIPS pentacene also included for comparison.
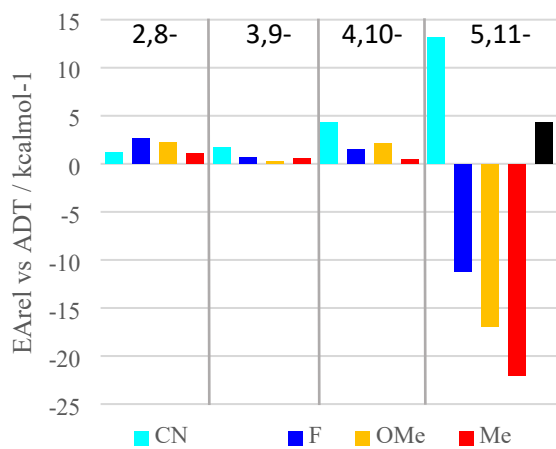
Figure S 57. Computed activation energies for different regioisomers of ADT, versus the unfunctionalized parent ADT. Calculations used the reaction path methodology described above.

X	Position	E_{rel}ADT (kcalmol)	E_{rel}EPO (kcalmol)	ΔE_{rel} (kJmol)
CN	2,8	6.9	-8.3	-63.5
	3,9	1.5	-13.2	-61.8
	4,10	0.6	-11.7	-51.6
F	2,8	9.6	17.2	31.8
	3,9	6.9	12.3	22.5
	4,10	0.3	6.3	25.3
Me	2,8	-9.2	3.9	55.1
	3,9	-8.8	3.8	52.7
	4,10	-5.5	6.0	48.2
OMe	2,8	-3.1	1.2	18.0
	3,9	-2.8	-1.2	6.8
	4,10	-0.1	4.1	17.6

Table S 2. Computed electronic energies relative to the 5,11- isomers with same X substituents for ADT and endoperoxides, and the reaction energy for endoperoxide formation relative to the 5,11- isomers.
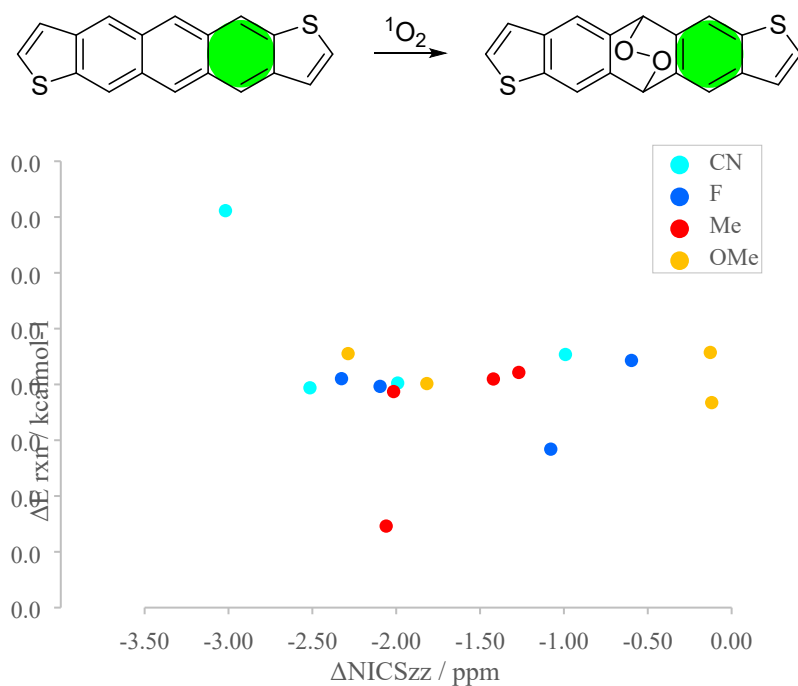
Figure S 58. Computed reaction energy for endoperoxide formation versus change in NICS zz values of the highlighted benzenoid ring. Different data points represent different substitution patterns on the ADT core.

References

1   M. M. Payne, S. R. Parkin, J. E. Anthony, C. C. Kuo and T. N. Jackson, *J. Am. Chem. Soc.*, 2005, **127**, 4986–4987.

2   S. Subramanian, K. P. Sung, S. R. Parkin, V. Podzorov, T. N. Jackson and J. E. Anthony, *J. Am. Chem. Soc.*, 2008, **130**, 2706–2707.

3   J. E. Anthony, S. Subramanian, S. R. Parkin, S. K. Park and T. N. Jackson, *J. Mater. Chem.*, 2009, **19**, 7984–7989.

4   K. J. Thorley, D. Dremann, H. F. Iqbal, S. R. Parkin, O. Jurchescu and J. E. Anthony, *Mol. Syst. Des. Eng.*, 2022, **7**, 374-380.

5   A. D. Platt, J. Day, S. Subramanian, J. E. Anthony and O. Ostroverkhova, *J. Phys. Chem. C*, 2009, **113**, 14006–14014.

6   J. E. Anthony, D. L. Eaton and S. R. Parkin, *Org. Lett.*, 2002, **4**, 15–18.

7   L. Abu-Sen, J. J. Morrison, A. B. Horn and S. G. Yeates, *Adv. Opt. Mater.*, 2014, **2**, 636–640.

8   M. J. Frisch, G. W. Trucks, H. B. Schlegel, G. E. Scuseria, M. A. Robb, J. R. Cheeseman, G. Scalmani, V. Barone, G. A. Petersson, H. Nakatsuji, X. Li, M. Caricato, A. V. Marenich, J. Bloino, B. G. Janesko, R. Gomperts, B. Mennucci, H. P. Hratchian, J. V. Ortiz, A. F. Izmaylov, J. L. Sonnenberg, D. Williams-Young, F. Ding, F. Lipparini, F. Egidi, J. Goings, B. Peng, A. Petrone, T. Henderson, D. Ranasinghe, V. G. Zakrzewski, J. Gao, N. Rega, G. Zheng, W. Liang, M. Hada, M. Ehara, K. Toyota, R. Fukuda, J. Hasegawa, M. Ishida, T. Nakajima, Y. Honda, O. Kitao, H. Nakai, T. Vreven, K. Throssell, Jr. J. A. Montgomery, J. E. Peralta, F. Ogliaro, M. J. Bearpark, J. J. Heyd, E. N. Brothers, K. N. Kudin, V. N. Staroverov, T. A. Keith, R. Kobayashi, J. Normand, K. Raghavachari, A. P. Rendell, J. C. Burant, S. S. Iyengar, J. Tomasi, M. Cossi, J. M. Millam, M. Klene, C. Adamo, R. Cammi, J. W. Ochterski, R. L. Martin, K. Morokuma, O. Farkas, J. B. Foresman and D. J. Fox, *Gaussian 16, Revision A.03*, Gaussian, Inc., Wallingford CT, 2016.

9   M. Moser, K. J. Thorley, F. Moruzzi, J. F. Ponder, I. P. Maria, A. Giovannitti, S. Inal and I. McCulloch, *J. Mater. Chem. C*, 2019, **7**, 5359–5365.